





ARTICLE

Parkin-independent mitophagy via Drp1-mediated outer membrane severing and inner membrane ubiquitination

Yumiko Oshima^{1,2}, Etienne Cartier^{1,2}, Liron Boyman^{1,3} , Nicolas Verhoeven^{1,2}, Brian M. Polster⁴ , Weiliang Huang⁵, Maureen Kane⁵, W. Jonathan Lederer^{1,3} , and Mariusz Karbowski^{1,2} 

Here, we report that acute reduction in mitochondrial translation fidelity (MTF) causes ubiquitination of the inner mitochondrial membrane (IMM) proteins, including TRAP1 and CPOX, which occurs selectively in mitochondria with a severed outer mitochondrial membrane (OMM). Ubiquitinated IMM recruits the autophagy machinery. Inhibiting autophagy leads to increased accumulation of mitochondria with severed OMM and ubiquitinated IMM. This process occurs downstream of the accumulation of cytochrome c/CPOX in a subset of mitochondria heterogeneously distributed throughout the cell (“mosaic distribution”). Formation of mosaic mitochondria, OMM severing, and IMM ubiquitination require active mitochondrial translation and mitochondrial fission, but not the proapoptotic proteins Bax and Bak. In contrast, in Parkin-overexpressing cells, MTF reduction does not lead to the severing of the OMM or IMM ubiquitination, but it does induce Drp1-independent ubiquitination of the OMM. Furthermore, high-cytochrome c/CPOX mitochondria are preferentially targeted by Parkin, indicating that in the context of reduced MTF, they are mitophagy intermediates regardless of Parkin expression. In sum, Parkin-deficient cells adapt to mitochondrial proteotoxicity through a Drp1-mediated mechanism that involves the severing of the OMM and autophagy targeting ubiquitinated IMM proteins.

Introduction

Mitochondria are central for numerous essential processes, including oxidative phosphorylation (OXPHOS), the tricarboxylic acid cycle, iron-sulfur cluster synthesis, and regulation of apoptosis (Friedman and Nunnari, 2014). Thus, it is not surprising that failure to maintain mitochondrial homeostasis contributes to the development of numerous disorders (Bonomini et al., 2015; Boyman et al., 2020; Currais, 2015; Kim et al., 2015).

In addition to other protective mechanisms, such as reactive oxygen species detoxification and mitochondrial fission and fusion (Boyman et al., 2020; Friedman and Nunnari, 2014; Scheibye-Knudsen et al., 2015), the ubiquitin (Ub) proteasome system (UPS), through degradation or control of outer mitochondrial membrane (OMM)-associated proteins or regulation of mitochondria-specific autophagy (mitophagy), is vital for the maintenance of mitochondrial function (Cherok et al., 2017; Heo et al., 2010; Karbowski and Youle, 2011; Liang et al., 2015). Mitochondria-associated components of the UPS, such as the E3 Ub ligases MARCH5 (Karbowski et al., 2007; Yonashiro et al.,

2006) and Parkin (Koyano et al., 2014; Narendra et al., 2008; Tanaka et al., 2010) and the deubiquitinase Usp30 (Bingol et al., 2014; Liang et al., 2015; Nakamura and Hirose, 2008), are essential for mitochondrial quality control. Among these proteins, the familial Parkinson’s disease-linked protein Parkin has been most extensively studied. Parkin translocates to terminally damaged mitochondria with low mitochondrial membrane potential ($\Delta\Psi_m$) and, through massive ubiquitination of OMM proteins, facilitates the mitochondrial accumulation of the autophagic machinery to remove the damaged mitochondria (Koyano et al., 2014; Lazarou et al., 2015).

Mitochondrial fission mediated by the GTPase dynamin-related protein 1 (Drp1) has been implicated in the control of Parkin-mediated mitophagy. The mechanisms by which Drp1 controls mitophagy include separation of low- $\Delta\Psi_m$ mitochondria from the functional mitochondrial network (Twig et al., 2008) or sequestration of misfolded mitochondrial proteins within a submitochondrial foci (Burman et al., 2017), facilitating

¹Center for Biomedical Engineering and Technology, University of Maryland School of Medicine, Baltimore, MD; ²Department of Biochemistry and Molecular Biology, University of Maryland School of Medicine, Baltimore, MD; ³Department of Physiology, University of Maryland School of Medicine, Baltimore, MD; ⁴Department of Anesthesiology and Center for Shock, Trauma, and Anesthesiology Research, University of Maryland School of Medicine, Baltimore, MD; ⁵Department of Pharmaceutical Sciences, University of Maryland School of Pharmacy, Baltimore, MD.

Correspondence to Mariusz Karbowski: mkarbowski@som.umaryland.edu.

© 2021 Oshima et al. This article is distributed under the terms of an Attribution-Noncommercial-Share Alike-No Mirror Sites license for the first six months after the publication date (see <http://www.rupress.org/terms/>). After six months it is available under a Creative Commons License (Attribution-Noncommercial-Share Alike 4.0 International license, as described at <https://creativecommons.org/licenses/by-nc-sa/4.0/>).

their elimination by autophagy. Drp1 recruitment to the mitochondria can also initiate the focal reduction of the $\Delta\Psi_m$ at a fission site, serving as a surveillance mechanism that separates damaged and functional mitochondria (Cho et al., 2019).

Substantial progress in mitophagy research was achieved using cells overexpressing exogenous Parkin. Cell lines frequently used in Parkin-mediated mitophagy research, including HeLa and HCT116 cells, either do not endogenously express Parkin or express it at low levels (Burman et al., 2017). Hence, these cells are frequently used as negative controls in studies of Parkin (Bingol et al., 2014; McLelland et al., 2018; Sarraf et al., 2013; Tanaka et al., 2010; Yoshii et al., 2011). Results obtained in Parkin-overexpressing cells were frequently verified in endogenous Parkin-expressing cells and animal models (Ashrafi et al., 2014; Cai et al., 2012; Chan et al., 2011). However, basal mitophagy is widespread in *Drosophila melanogaster* and mouse tissues of high metabolic demand but minimally affected by either the loss of Parkin (Lee et al., 2018) or the Parkin cofactor PTEN-induced putative kinase 1 (PINK1; McWilliams et al., 2018), respectively. Furthermore, a relatively normal phenotype of the Parkin knockout mouse (Perez and Palmiter, 2005), and data showing that mitophagy in cancer cells does not require Parkin (Villa et al., 2017), suggest that yet-to-be identified mechanisms contribute to the elimination of dysfunctional mitochondria in both Parkin-deficient and Parkin-expressing cells. Mitochondrial fission also controls mitophagy in Parkin-deficient cells (Kageyama et al., 2014; Yamada et al., 2018), but the mechanism remains elusive.

Mitochondrial translation defects have been linked to mitochondrial decline in aging and the development of multiple diseases (Battersby and Richter, 2013; Canet-Avilés et al., 2004; Sheth et al., 2014; Smits et al., 2010). Reduced accuracy of this process was implicated in shortening of the replicative lifespan of mammalian and yeast cells (Breitenbach et al., 2014; Caballero et al., 2011; Suhm et al., 2018) and induction of mitochondrial unfolded protein response (Sheth et al., 2014). Cancer cell survival also depends on mitochondrial translation efficiency (Skrtić et al., 2011). However, the role and mechanism by which reduced mitochondrial translation fidelity (MTF) affects mitochondrial ubiquitination and mitophagy, and the degree to which Drp1 and mitochondrial fission contribute to this process, are not well understood.

Here, we report that in response to mitochondrial proteotoxicity, induced by reduced MTF, cells use a novel mitochondrial quality control Parkin-independent mechanism. This process includes the severing of the OMM, inner mitochondrial membrane (IMM) ubiquitination, and degradation of defective mitochondrial fragments by mitophagy.

Results

Drp1-dependent mosaic distribution of cytochrome c in cells with reduced fidelity of mitochondrial translation

Maintaining rates and/or fidelity of translation of mitochondrial DNA (mtDNA)-encoded proteins is vital for cell function (Canet-Avilés et al., 2004; Skrtić et al., 2011; Smits et al., 2010). However, how mitochondria adapt to abnormal mitochondrial

translation is not well understood. To investigate this question, first we applied actinonin (Acn), a compound that inhibits mitochondrial peptide deformylase, stalls mitochondrial ribosomes, and thereby induces defects in MTF and accumulation of damaged mtDNA-encoded proteins on the IMM (Richter et al., 2013; Richter et al., 2015).

As reported previously (Richter et al., 2013; Richter et al., 2015), fragmented mitochondria were detected in ~100% of Acn-treated human colon carcinoma HCT116 cells (Fig. 1 B). We also found that in contrast to control cells (Fig. 1 A), some mitochondria in Acn-treated cells displayed higher while some showed lower fluorescence intensity of the intermembrane space (IMS) protein cytochrome c (hereafter termed as “mosaic distribution” of cytochrome c; Fig. 1 B). On the other hand, the distribution of markers of the OMM (Tom20) and caseolytic mitochondrial matrix peptidase proteolytic subunit (ClpP) did not appear to be affected (Fig. 1 B). Mosaic distribution of cytochrome c was initially detected in Acn-treated cells after 2 h of treatment ($14.1 \pm 2.5\%$ of cells), detected in nearly all the cells after 4 h ($97.4 \pm 3.2\%$), and further extended to ~100% of the cells at 6 h (see Fig. 1 C). The data also show a gradual increase in the abundance of high-cytochrome c mitochondria within a cell. In WT HCT116 cells, the high-cytochrome c mitochondria represented $1.5 \pm 1\%$, $11.9 \pm 6.5\%$, and $16.0 \pm 6.2\%$ of total mitochondrial network areas at 2, 4, and 6 h of Acn treatment, respectively (Fig. 1 D). Acn-induced mosaic distribution of cytochrome c was detected in all tested cell types, including HCT116 cells (Fig. 1, B and G), human neuroblastoma M17 (Fig. S1, A and B), HeLa cells (Figs. 1 G and S1 D), and mouse embryonic fibroblasts (MEFs; Figs. 1 G and S2 A).

A potential explanation for the mosaic distribution of cytochrome c is that Acn triggered cytochrome c release from a subset of mitochondria. However, this phenotype was detected in Acn-treated HCT116 cells deficient in Bax and Bak (Bax/Bak double-knockout [DKO] cells; Figs. 1 G and S1 F), Bcl-2 family proteins instrumental in apoptotic OMM permeabilization and release of cytochrome c from the mitochondria (Nechushtan et al., 1999; Wang and Youle, 2012). Furthermore, we did not detect Bax accumulation on the mitochondria in Acn-treated cells (Fig. S3 A). On the other hand, cytochrome c release and mitochondrial accumulation of Bax occurred in WT, but not Bax/Bak DKO, cells treated with the apoptosis inducer ABT-737 (Fig. S3, B–E). Moreover, caspase 9 and PARP1 cleavage, markers of mitochondria-dependent apoptosis, were detectable at 48 h of treatment with Acn (Fig. S3 F). ABT-737 induced much stronger caspase 9 and PARP1 cleavage at 12 h of treatment. Thus, it is unlikely that apoptotic OMM permeabilization contributes to the mosaic distribution of cytochrome c. Furthermore, the fluorescence signal of cytochrome c was markedly elevated in mosaic mitochondria compared with mitochondria from control cells, suggesting that reduced MTF could induce asymmetrical redistribution of cytochrome c between distinct mitochondria.

We found a uniform distribution of cytochrome c in control and Acn-treated, mitochondrial fission factor dynamin-like protein 1 (Drp1) knockout HCT116 (Drp1^{-/-}; Fig. 1, E–G) and Drp1^{-/-} HeLa (Fig. 1 G) cells and Drp1^{-/-} MEFs (Figs. 1 G and S2 E), indicating that Drp1 and, likely, mitochondrial fission are

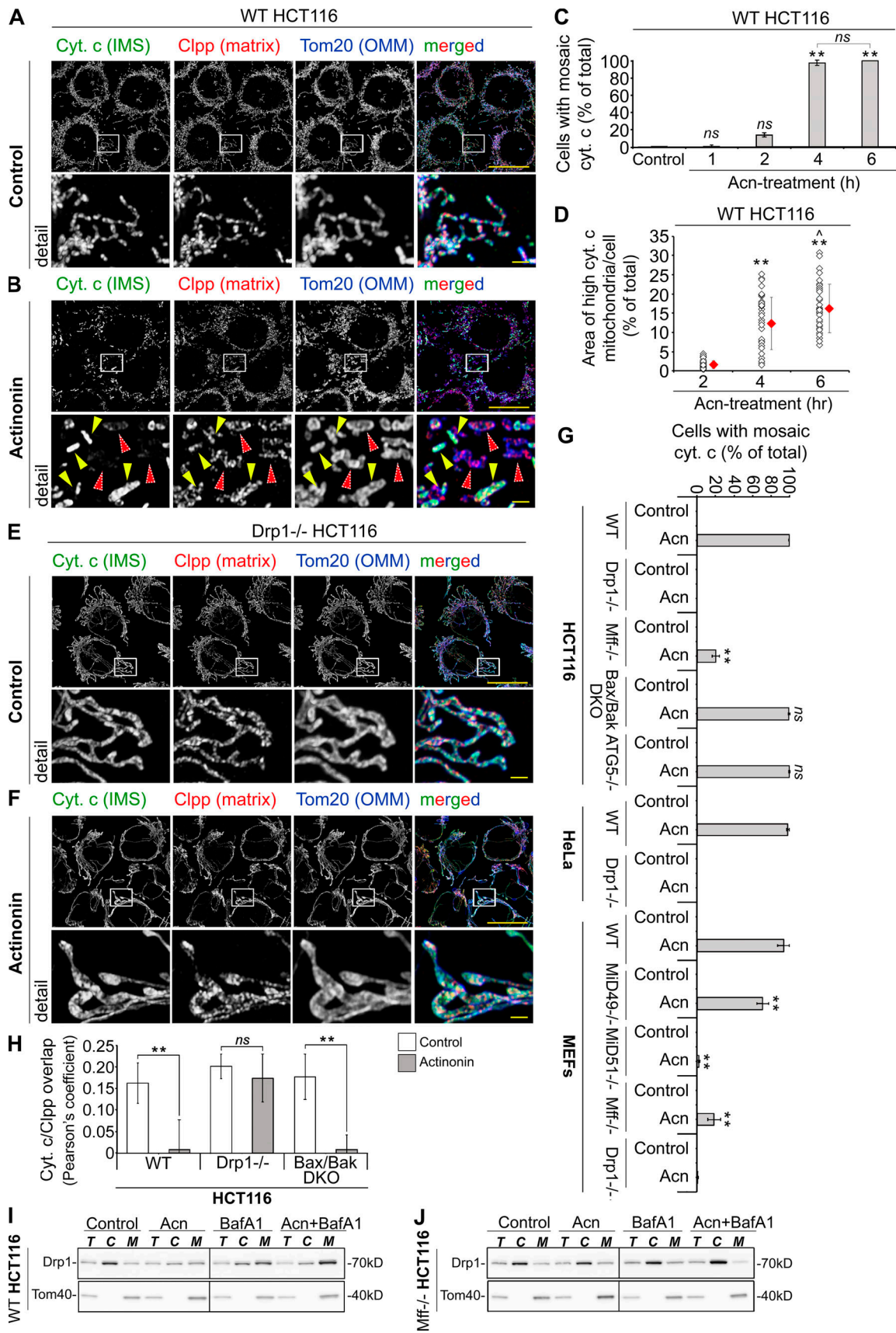


Figure 1. **Drp1-dependent mosaic distribution of cytochrome c in cells with reduced MTF.** (A, B, E, and F) WT (A and B) and Drp1^{-/-} (E and F) HCT116 cells were treated with DMSO (control; A and E) or Acn (B and F) for 6 h, followed by immunostaining to detect cytochrome c (IMS marker, green), ClpP (matrix

marker; red), and Tom20 (OMM marker; blue) and Airyscan superresolution image acquisition. Yellow arrowheads in B point to the high-cytochrome c mitochondria, and red arrowheads in B indicate the “low”-cytochrome c mitochondria. Scale bars represent 20 μm (2 μm in detail images). **(C)** Number of cells with high-cytochrome c mitochondria was quantified in cells treated as shown in the figure. Data represent mean \pm SD of $n = 3$. In each experiment, triplicates of 150 cells were counted. **, $P < 0.01$ versus control; *ns* indicates nonsignificant; Kruskal–Wallis with Dunn post-hoc analysis ($\alpha = 0.05$). **(D)** Relative area of high-cytochrome c mitochondria per cell was quantified in WT HCT116 cells treated with Acn as indicated in the figure and expressed as a percentage of total mitochondria/cell. Tom20 signal was considered as a 100%. $n = 50$. **, $P < 0.01$ versus 2 h; \wedge , $P < 0.01$ versus 4 h; one-way ANOVA with Bonferroni correction ($\alpha = 0.05$). **(G)** Quantification of cells with mosaic cytochrome c distribution. Cells indicated in the figure were treated with DMSO (vesicle; control) or Acn for 6 h. Data represent mean \pm SD; $n = 3$, $n = 100$ cells per condition per each N. **, $P < 0.01$ versus WT Acn in each cell type; *ns* indicates nonsignificant; one-way ANOVA with Bonferroni correction ($\alpha = 0.05$). **(H)** Overlap between cytochrome c and ClpP in control and Acn-treated WT, Drp1^{-/-}, and Bax/Bak DKO HCT116 cells was estimated from maximum intensity projection images (as in A, B, E, and F). The values are shown as Pearson’s correlation coefficient. Data are represented as mean \pm SD; $n = 30$ cells per condition (data pulled from $n = 2$ independent experiments). **, $P < 0.01$ versus control in each group; *ns* indicates nonsignificant; one-way ANOVA with Bonferroni correction ($\alpha = 0.05$). **(I and J)** WT (I) and Mff^{-/-} (J) HCT116 cells treated as indicated in the figure were subjected to cell fractionation and Western blot analysis to detect subcellular localization of Drp1. Tom40 was used as a loading control. C, cytosol (post-mitochondrial supernatants, including LMs); Cyt. C, cytochrome c; M, mitochondria-enriched HM fractions, T, total cell lysate.

required for mosaic distribution of cytochrome c. Consistent with this, expression of dominant-negative Drp1 mutant (Drp1^{K38A}; Smirnova et al., 2001) also inhibited mosaic distribution of cytochrome c in Acn-treated WT cells (Fig. S4, A and C). Colocalization analyses revealed significant decreases in the overlap between cytochrome c and ClpP in Acn-treated WT and Bax/Bak DKO cells, but not in Drp1^{-/-} cells (Fig. 1 H).

We tested the degree to which depletion of the OMM-localized receptors of Drp1, MiD49, MiD51, and Mff affects mosaic cytochrome c distribution in MEFs. Acn-induced mosaic cytochrome c distribution was detected in 83.3 \pm 7.4% of WT MEFs, 50.1 \pm 7.2% of MiD49^{-/-} MEFs, 4.2 \pm 2.2% of Mff^{-/-} MEFs, 1.6 \pm 0.4% of MiD51^{-/-} MEFs, and 0.8 \pm 0.2% of Drp1^{-/-} MEFs (Figs. 1 G and S2). Thus, formation of mosaic cytochrome c mitochondria requires Drp1 and the Drp1 receptors Mff and MiD51, indicating that mitochondrial fission controls this process. Further supporting this conclusion are our findings showing that Drp1 recruitment to the mitochondria occurs in Acn-treated WT, but not Acn-treated Mff^{-/-}, HCT116 cells (Fig. 1, I and J).

Inhibition of mitochondrial translation abrogates mosaic distribution of cytochrome c

In contrast to the observed effects of Acn, treatments with other compounds affecting mitochondrial function did not lead to mosaic distribution of cytochrome c (Fig. 2 A). Such tested treatments include the uncoupler carbonyl cyanide 4-(trifluoromethoxy) phenylhydrazone (FCCP), a mixture of oligomycin and antimycin A (OA; inhibitors of mitochondrial ATP synthase and cytochrome c reductase, respectively), rotenone (an inhibitor of mitochondrial NADH, ubiquinone oxidoreductase), and chloramphenicol (CP; an inhibitor of mitochondrial translation). Furthermore, FCCP and CP inhibited mitochondrial mosaicism in Acn-treated cells (Fig. 2 A; and Fig. S4, E–K). Therefore, not a general decline in mitochondrial function but instead the reduced MTF specifically causes the mosaic distribution of cytochrome c in Acn-treated cells.

Supporting the data indicating that Acn inhibits mitochondrial translation checkpoint leading to accumulation of mtDNA-encoded proteins on the IMM (Richter et al., 2015), we also found that Acn treatment led to accumulation of IMM proteins Cox2, ATP8, and NDUFB8 (Fig. 2, B and F). Inhibition of mitochondrial translation with CP reduced Acn-dependent accumulation of these proteins (Fig. 2 B) and prevented formation of

mosaic cytochrome c mitochondria (Fig. 2 A; and Fig. S4, E–K). Formation of mosaic cytochrome c mitochondria was almost completely inhibited in Acn-treated mtDNA-depleted HCT116 cells ($\rho 0$ cells; Fig. 2, C–E), verifying a critical role for reduced MTF. Specifically, only 3.75 \pm 1.71% of Acn-treated $\rho 0$ cells as compared with 98.5 \pm 1.29% of Acn-treated WT HCT116 cells showed mosaic cytochrome c distribution (Fig. 2 E). Western blotting confirmed depletion of mtDNA-encoded proteins in HCT116 $\rho 0$ cells and their accumulation in WT HCT116 cells treated with Acn for 4hr (Fig. 2 F). Although, an accessory subunit of complex I, NDUFB8 is encoded by nuclear gene, it has been also reduced in HCT116 $\rho 0$ cells (Fig. 2 F). In agreement with similar observations commonly reported by others (Gammage et al., 2014; Moretton et al., 2017) these data suggest that NDUFB8 stability is affected by expression of mitochondria-encoded proteins. The increase of NDUFB8 in Acn-treated cells (Fig. 2, B and F) is likely to reflect its balancing function in complex I assembly and stability (Piekutowska-Abramczuk et al., 2018). To further test the hypothesis that abnormal accumulation of proteins on the IMM causes mosaic distribution of cytochrome c, we ectopically expressed HA-tagged accessory subunit of complex I NDUFA12 (NDUFA12-HA) in WT HCT116 and HeLa cells and Drp1^{-/-} HCT116 cells (Fig. 2, G–J). Expression of NDUFA12-HA induced formation of mosaic cytochrome c in 69.8 \pm 8.7% and 59.9 \pm 15.3% of transfected WT HCT116 (Fig. 2, G and I) and WT HeLa cells (Fig. 2 I), respectively. None of the NDUFA12-HA-transfected Drp1^{-/-} HCT116 cells displayed mosaic cytochrome c (Fig. 2, H and I). This evidence suggests that reduced MTF and the resulting accumulation of proteins on the IMM induce mosaic distribution of cytochrome c in a Drp1-dependent manner.

The data also show that Acn-induced changes in reporters of mitochondrial functional decline, such as increased short Opal isoform levels and enhanced autophagy (including p62 degradation or formation of lipidated LC3II), are inhibited by cotreatment with CP or depletion of mtDNA (Fig. 2, B, F, L, M, O, and P). Interestingly, reduction in Drp1, apparent in Acn-treated cells, was also suppressed by CP and mtDNA depletion (Fig. 2, B, F, K, and N).

Effect of reduced MTF on cytochrome c distribution in living cells

Live-cell time-lapse imaging was applied to test the effect of reduced MTF and $\Delta\Psi_m$ dissipation on cytochrome c distribution

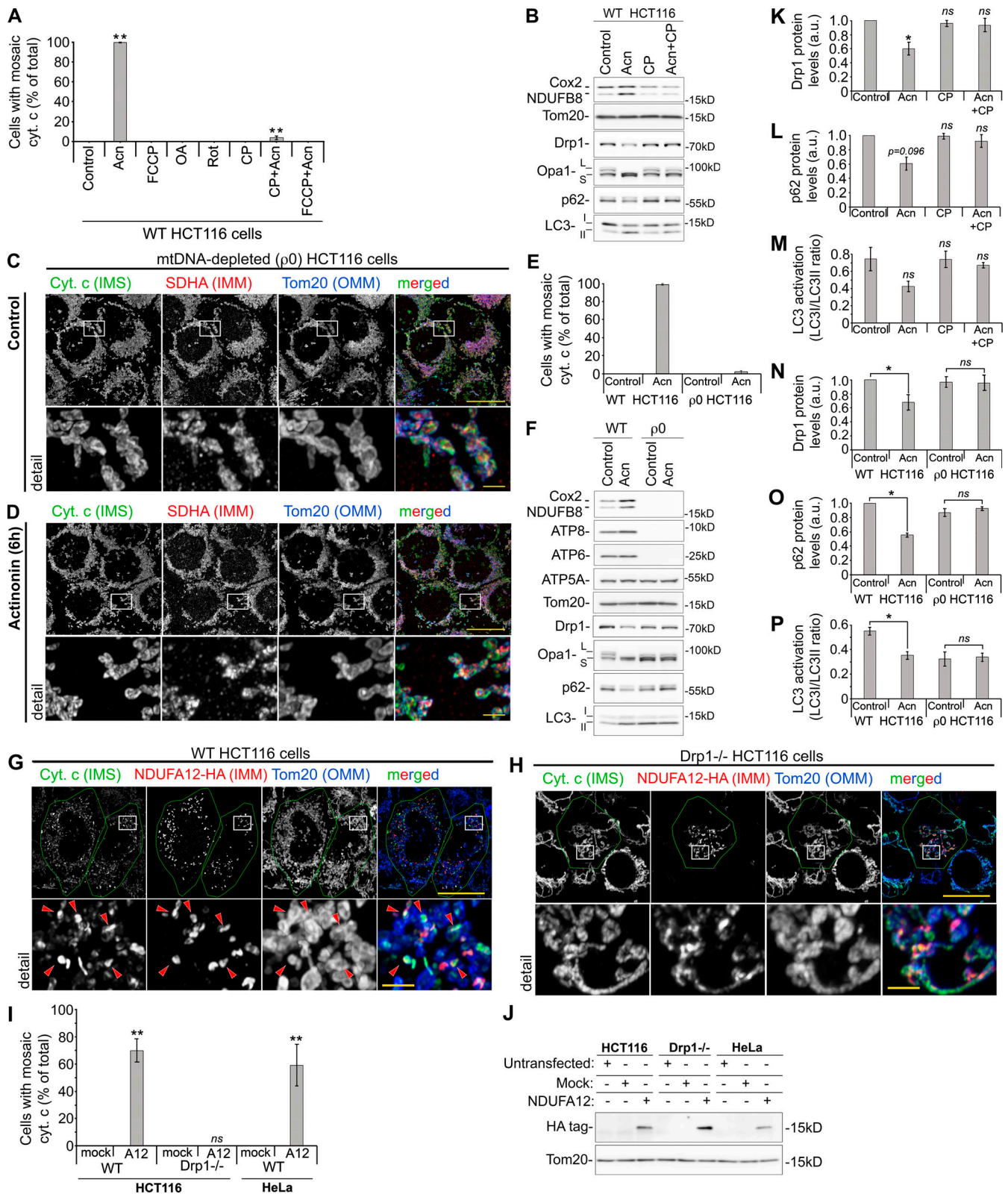


Figure 2. **Mosaic cytochrome c distribution is induced by abnormal accumulation of the proteins on the IMM.** (A) Quantification of cells with mosaic cytochrome c in WT HCT116 cells treated with the indicated compounds for 6 h. Data are represented as mean \pm SD; $n = 4$, $n = 100$ cells per condition were counted in each experiment. **, $P < 0.01$ versus control (all other groups were nonsignificant); one-way ANOVA with Bonferroni correction ($\alpha = 0.05$). (B) Total cell lysates of WT HCT116 cells treated as indicated in the figure for 6 h were analyzed by Western blot. Tom20 was used as a loading control. (C and D) mtDNA-depleted HCT116 cells were treated with DMSO (control; C) or Acn (D) for 6 h, followed by immunostaining for cytochrome c (cyt. c; green), SDHA (red), and Tom20 (blue) and Airyscan image acquisition. Detail images are from areas outlined with white rectangles. Scale bars represent 20 μ m (2 μ m in detail).

images). **(E)** Number of cells with mosaic cytochrome c distribution in WT and mtDNA-depleted HCT116 cells treated with DMSO (control) or Acn for 6 h. Data represent mean \pm SD; $n = 4$, $n = 150$ cells per condition per each independent experiment. **(F)** Total cell lysates of WT and mtDNA-depleted HCT116 cells treated with DMSO (vehicle) or Acn for 6 h were subjected to Western blotting as shown in the figure. Tom20 was used as a loading control. **(G and H)** WT (G) and Drp1^{-/-} (H) HCT116 cells transfected with NDUFA12-HA were immunostained to detect cytochrome c (cyt. c; green), Tom20 (blue), and HA-tag (red). Red arrowheads in G indicate high-cytochrome c mitochondria. Detail images are from areas outlined with white rectangles. Scale bars represent 20 μ m (2 μ m in detail images). **(I)** Quantification of mosaic cytochrome c mitochondria in mock-transfected cells and cells transfected with NDUFA12-HA (A12). Data are represented as mean \pm SD; $n = 4$, $n = 150$ cells per condition (WT and Drp1^{-/-} HCT116 cells) and $n = 3$, $n = 150$ cells per condition (HeLa cells). **, $P < 0.01$ versus “mock” in each cell type; *ns* indicates nonsignificant; one-way ANOVA with Bonferroni correction ($\alpha = 0.05$). **(J)** Expression levels of NDUFA12-HA in WT and Drp1^{-/-} HCT116 and WT HeLa cells. Tom20 was used as a loading control. **(K–P)** Expression levels of Drp1 (K and N), p62 (L and O), and LC3-I/LC3II ratio (M and P) in WT HCT116 cells treated with Acn, CP, or Acn plus CP (K–M) or mtDNA-depleted HCT116 cells treated with Acn (N–P). Data are represented as mean \pm SD; $n = 3$. *, $P < 0.05$ versus control; *ns* indicates nonsignificant; Kruskal–Wallis with Dunn post-hoc analysis ($\alpha = 0.05$; K–M) or Wilcoxon rank-sum test (N–P).

in living cells. In these experiments, we used HeLa cells, which are larger and flatter than HCT116 cells. The data show the expected uniform distribution of GFP-tagged cytochrome c (cyt. c-GFP) and RFP-tagged marker of mitochondrial matrix (mito-RED) at the early time points of Acn treatment. This was followed by the formation of mitochondria with high fluorescence intensity of cyt. c-GFP in Acn-treated cells, starting between 120 and 180 min and continuing until 300 min, when the image acquisition was stopped (Fig. 3, A and D; and Video 1). The formation of high cyt. c-GFP-intensity mitochondria occurred to a much lesser degree in Drp1^{-/-} (Fig. 3, B and E; and Video 2) and Mff^{-/-} cells (Fig. 3 F and Video 3). The number of high cyt. c-GFP mitochondria per cell at 300 min with Acn was 11.36 ± 2.54 in WT, 0.18 ± 0.40 in Drp1^{-/-}, and 0.37 ± 0.74 in Mff^{-/-} cells (Fig. 3, D–F). The formation of high cyt. c-GFP-intensity mitochondria in Drp1^{-/-} cells was substantially restored by ectopic expression of mCherry-tagged Drp1 (Drp1-mCherry; Fig. 3 E and Video 4; 9.1 ± 4.4 high cyt. c-GFP mitochondria at 300 min with Acn). High cyt. c-GFP-intensity mitochondria were not detected in WT or Drp1^{-/-} cells treated with DMSO (control; Fig. 3, D and E) or in WT cells treated with FCCP (Fig. 3, C and D; and Video 5). Supporting the critical role for MTF in the process, inhibition of mitochondrial translation with CP markedly reduced the formation of high cyt. c-GFP mitochondria in WT cells (Fig. 3 D and Video 6; 1.25 ± 1.39 high cyt. c-GFP mitochondria at 300 min).

We also tested the connection between the formation of mosaic cytochrome c and changes in $\Delta\Psi_m$. Cells transfected with cyt. c-GFP were labeled with tetramethylrhodamine methyl ester (TMRM), a cell-permeant cationic fluorescent probe that accumulates preferentially in mitochondria with undamaged-highly polarized $\Delta\Psi_m$, followed by time-lapse imaging in the presence of Acn or Acn plus CP. Formation of high-cytochrome c mitochondria in Acn-treated cells occurs close in time to initial reduction of $\Delta\Psi_m$, which starts at 120–180 min (Figs. 3 G and S5 and Video 7). On the other hand, no $\Delta\Psi_m$ decline was detected in cells cotreated with Acn and CP, indicating that active mitochondrial translation with reduced fidelity specifically drives $\Delta\Psi_m$ alterations (Fig. 3 G and Video 6). After 300 min of treatment with Acn, all high cyt. c-GFP mitochondria showed no detectable TMRM fluorescence (Figs. 3 H and S5 and Video 7). Other mitochondria, without high cyt. c-GFP, preserved normal or slightly reduced TMRM staining. Thus, while direct dissipation of $\Delta\Psi_m$ by treatment with FCCP does not induce formation of mosaic cytochrome c mitochondria, reduction of MTF leads to $\Delta\Psi_m$ decline.

Reduced MTF induces Drp1-mediated severing of the OMM and mitochondrial ubiquitination

Acn treatment induces Ub-mediated mitophagy in E3 Ub ligase Parkin-overexpressing cells (Burman et al., 2017) or enhances this process in amyloid- β and tau models of Alzheimer’s disease (Fang et al., 2019). It has been proposed that in Parkin-mediated mitophagy Acn induces misfolding of mitochondrial matrix and/or IMM proteins and that their removal is facilitated by focal localization of Parkin and subsequent recruitment of autophagy adaptors to Parkin-positive OMM foci (Burman et al., 2017). We explored the degree to which Acn-induced reduction of MTF affects mitochondrial ubiquitination.

Diffused cytosolic localization and nuclear foci of Ub were detected in control cells (Fig. 4, A and E) and cells treated with CP (Fig. 4 C). In contrast, Acn induced formation of circular Ub-positive structures invariably associated with mitochondria (Fig. 4, B and G). The number of mitochondria-associated circular Ub structures was over threefold higher in Acn-treated mitophagy-deficient ATG5^{-/-} cells than in Acn-treated WT cells (1.35 ± 0.22 per cell in WT versus 4.39 ± 0.22 in ATG5^{-/-} cells; Fig. 4 I), suggesting that in WT cells, autophagy clears these structures. Consistent with this, cotreatment of WT cells with Acn and the autophagy inhibitor bafilomycin A1 (BafA1) resulted in an increase in the number of mitochondria-associated circular Ub to 4.27 ± 0.15 per cell (Fig. 4 I). Circular mitochondrial ubiquitination was not detected in CP-treated cells (Fig. 4, C and I) and was reduced in Acn- and CP-cotreated WT (0.43 ± 0.19) and ATG5^{-/-} (0.57 ± 0.21) cells (Fig. 4, D and I). Supporting the specific role of reduced MTF, no circular mitochondrial ubiquitination was detected in cells treated with the OXPHOS inhibitors rotenone or OA or the uncoupler FCCP (Fig. 4 I). In contrast to WT and ATG5^{-/-} cells, no circular mitochondrial Ub structures were detectable in Drp1^{-/-} cells treated with Acn or BafA1 or cotreated with Acn plus BafA1 (Fig. 4, E, F, and I). Furthermore, expression of a dominant-negative Drp1^{K38A} (Smirnova et al., 2001) reduced circular mitochondrial ubiquitination in Acn-treated WT and ATG5^{-/-} cells (Fig. S4, B and D). Thus, Drp1 and mitochondrial fission are crucial for formation of mitochondrial circular Ub structures.

Notably, circular Ub did not colocalize with OMM markers, including Tom20, Tom40, and Fis1, but it was invariably associated with the subset of mitochondria showing discontinuous fluorescence signals of these OMM proteins (Fig. 4, G and H; and Fig. S6, A and B). All tested mitochondria with discontinuous OMM ($n = 150$) were deficient in cytochrome c (Fig. 4 J). Cell

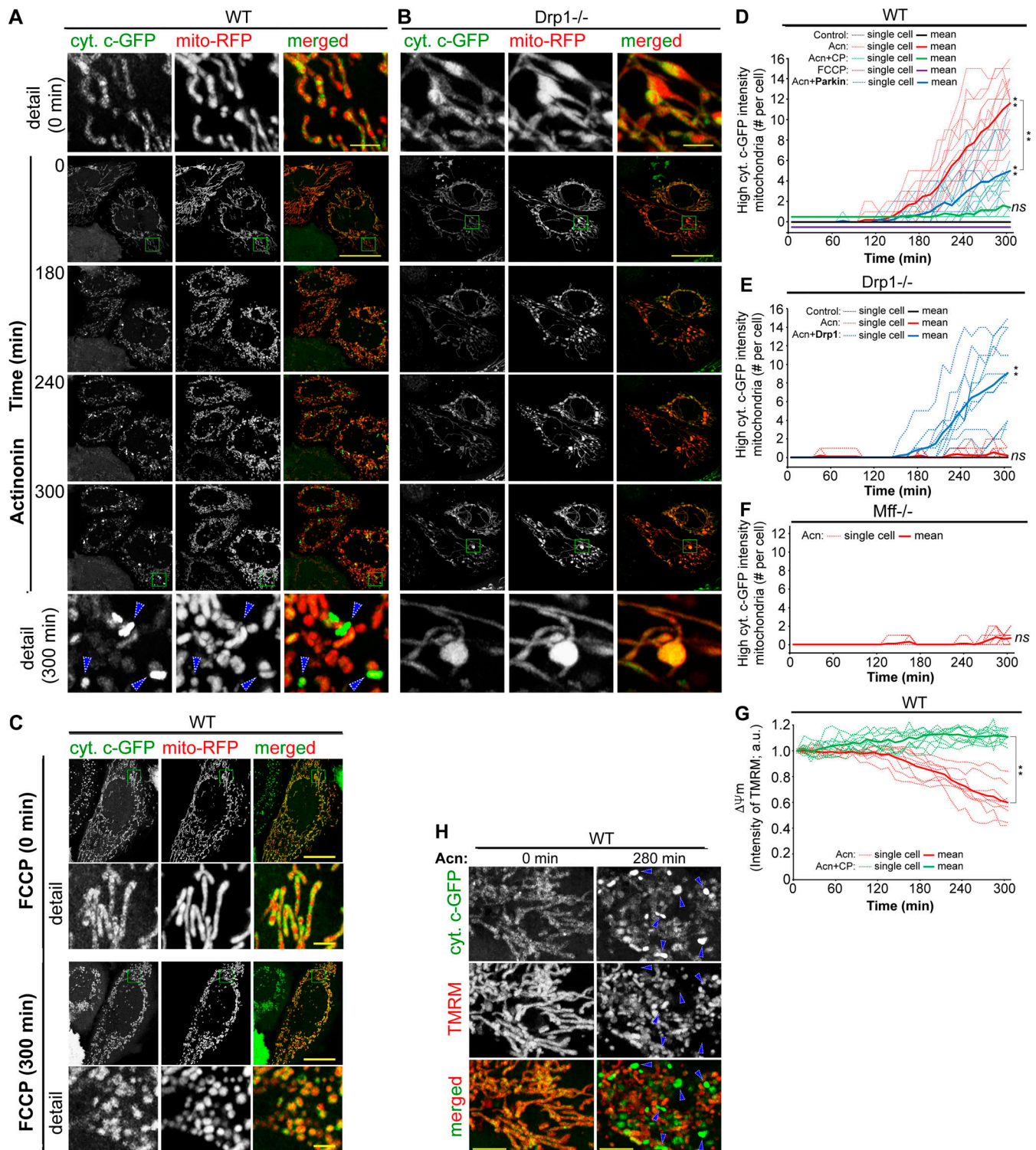


Figure 3. Time-lapse imaging of cytochrome c-GFP in Acn-treated WT and Drp1^{-/-} cells. (A–C) WT (A and C) and Drp1^{-/-} (B) HeLa cells cotransfected with cytochrome c-GFP (green in A–C) and mito-RFP (red in A–C) treated with Acn (A and B) or FCCP (C) were subjected to time-lapse imaging for up to 300 min. Detail images at time 0 min and 300 min in A–C are from areas outlined with green rectangles. Arrowheads in A point to high cytochrome c-GFP intensity mitochondria and corresponding mito-RFP signal. Scale bars represent 20 μ m (2 μ m in detail images) in A and B and 10 μ m (1 μ m in detail images) in C. (D–F) Formation of high cytochrome c-GFP intensity mitochondria in WT (D), Drp1^{-/-} (E), and Mff^{-/-} (F) HeLa cells over time in several time-lapse experiments were quantified. Data represent $n = 3$ (6 cells) for control WT cells, $n = 8$ (11 cells) for Acn-treated WT cells, $n = 5$ (8 cells) for Acn plus CP-treated WT cells, $n = 5$ (8 cells) for FCCP-treated cells, $n = 4$ (10 cells) for Acn-treated Parkin-mCherry-expressing WT cells, $n = 6$ (11 cells) for Acn-treated Drp1^{-/-} cells, $n = 5$ (10 cells) for Drp1-mCherry-expressing Acn-treated Drp1^{-/-} cells, and $n = 5$ (8 cells) for Acn-treated Mff^{-/-} cells. **, $P < 0.01$ versus control at 300 min; ns indicates nonsignificant; one-way ANOVA with Bonferroni correction ($\alpha = 0.05$). To facilitate data evaluation in D, the values for control were shifted 0.5 units down, and the values for Acn plus CP were shifted 0.5 units up. (G) Fluorescence intensity of TMRM in WT cells treated with Acn or Acn plus CP for up to 300 min was quantified and plotted as function

of time. The TMRM fluorescence values at time 0 min (the first image in each series) were taken as 1. Data represent $n = 3$ ($n = 10$). **, $P < 0.01$ at 300 min; two-tailed Student's *t* test. **(H)** Patterns of cyt. *c*-GFP (green) and TMRM (red) localization and intensity in Acn-treated WT cells. The same area of a typical cell at 0 min and at 280 min with Acn is shown. Arrowheads point to some high cyt. *c*-GFP intensity mitochondria and corresponding TMRM signal. Scale bars represent 3 μm .

fractionation and Western blot support the imaging data. We found that treatment with Acn leads to enrichment of mitochondrial proteins, including ATP5A, ATP8, and Opa1, in light membrane (LM) fractions (Fig. 4 K; see also Figs. 5 A and 6 D), indicating that an increased subset of mitochondria copurifies with LM fractions (hereafter denoted as “light mitochondria”). Since, in contrast to other tested mitochondrial markers, light mitochondria in Acn-treated cells did not show any cytochrome *c* enrichment compared with light mitochondria in control cells (Fig. 4 K), these data suggest that circular Ub could be specifically associated with the light mitochondria, some of which showed large openings in the OMM (hereafter denoted as “severed OMM”).

Circular ubiquitination and OMM severing were also detected in Bax/Bak DKO cells (Fig. S1, G and H), indicating that unlike in apoptosis, where Bax and Bak are obligatory for the OMM rupture (Große et al., 2016; McArthur et al., 2018), OMM severing in Acn-treated cells does not require these proteins. Furthermore, while less pronounced than in HCT116 cells, circular ubiquitination of mitochondria with severed OMM was also detected in HeLa cells treated with Acn (0.67 ± 0.13 per cell) and Acn plus BafA1 (1.33 ± 0.27 per cell; Fig. S6, C and D). Because HeLa cells do not express Parkin (Fig. S6 E; Burman et al., 2017), OMM severing and circular ubiquitination of the IMM do not appear to require this protein.

Mitochondrial ubiquitination in cells with reduced MTF

We investigated mitochondrial ubiquitination in cells with reduced MTF (Fig. 5). The data show slightly increased ubiquitination of LM fractions from Acn-treated WT and ATG5^{-/-} cells as compared with DMSO-treated (control) cells (Fig. 5, A and B), while ubiquitination of mitochondria-enriched heavy membrane (HM) fractions was slightly reduced (Fig. 5 A). Furthermore, a slight reduction of Ub K48 chains (Fig. 5 C) and an increase in Ub K63 chains (Fig. 5 D) were apparent in LM fractions from Acn-treated cells, suggesting that light mitochondria in these cells could be targeted by autophagy.

To identify the mitochondrial compartment that is ubiquitinated in Acn-treated cells, we analyzed single *z*-section images from cells immunostained for Ub, together with markers for distinct mitochondrial compartments: Tom20 (OMM; Fig. 5, E and H), Tim23 (IMM; Fig. 5, F and H), succinate dehydrogenase complex flavoprotein subunit A (SDHA; IMM/matrix; Fig. 5 H), and ClpP (matrix; Fig. 5, G and H). The localization of Ub relative to Tom20, Tim23, SDHA, and ClpP was estimated from mitochondria showing the OMM severing (as in Fig. 4, G and J; and Fig. 5, E–G). Positions of the fluorescence peaks of Tom20, Tim23, SDHA, and ClpP along the fluorescence profiles, relative to the fluorescence peaks of Ub (exemplified in right-side panels in Fig. 5, E–G), were considered to represent the distance between the tested proteins. The assay revealed high colocalization

between Ub and Tim23 (distance between fluorescence peaks, $-0.04 \pm 0.08 \mu\text{m}$) and Ub and SDHA ($-0.05 \pm 0.08 \mu\text{m}$), but not between Ub and Tom20 ($0.23 \pm 0.16 \mu\text{m}$) or Ub and ClpP ($-0.38 \pm 0.19 \mu\text{m}$; Fig. 5 H). Thus, circular Ub in Acn-treated cells likely represents the ubiquitination of IMM protein (hereafter denoted as “IMM ubiquitination”).

Reduced MTF induces ubiquitination of the IMM/IMS proteins TRAP1 and CPOX

To identify mitochondrial proteins that are ubiquitinated in cells with reduced MTF, membrane fractions obtained from control (DMSO-treated) and Acn-treated WT and ATG5^{-/-} HCT116 cells were subjected to mass spectrometry. The localization probabilities of ubiquitination sites marked by diglycine were computed using a ptmRS algorithm (Taus et al., 2011). We identified five mitochondrial proteins showing significantly increased ubiquitination in samples obtained from Acn-treated as compared with control cells (Fig. 6 A; see Data S1 for the whole dataset). Four of these proteins (inorganic phosphatase 2, NDUFB10, oxygen-dependent coproporphyrinogen-III oxidase [CPOX], and TNF receptor-associated protein 1 [TRAP1; also known as HSP75]) localize to the mitochondria (Grandchamp et al., 1978; Medlock et al., 2015; Pridgeon et al., 2007), while p62 is an adaptor implicated in Ub-dependent mitophagy (Yamada et al., 2018). To verify the mass spectrometry data, we applied Ub pull-down under denaturing conditions (Fig. 6, B–D). Mitochondria-enriched HM and light mitochondria fractions from DMSO- or Acn-treated WT (Fig. 6, B and D) or ATG116^{-/-} (Fig. 6, C and D) cells were analyzed. While we could not confirm the ubiquitination of inorganic phosphatase 2 or NDUFB10 by pull-down assay (data not depicted), increased ubiquitination of CPOX and TRAP1 was detected in light mitochondria fractions from Acn-treated ATG5^{-/-} cells (Fig. 6 C), but not Acn-treated WT cells (Fig. 6 B). Considering a several fold increase in mitochondria-associated circular Ub in Acn-treated ATG5^{-/-} cells compared with Acn-treated WT cells (Fig. 4 I), it is likely that detection of ubiquitinated CPOX and TRAP1 in ATG5^{-/-} cells, but not WT cells, reflects circular ubiquitination of the IMM. Supporting this notion, CPOX and TRAP1 were reported to bind the IMS-facing side of the IMM (Grandchamp et al., 1978; Pridgeon et al., 2007) and therefore are exposed to the cytosol in mitochondria with severed OMM. Submitochondrial localization of CPOX (Fig. 6, E–G) and TRAP1 (Fig. S6 F) in control and Acn-treated cells was analyzed using immunofluorescence and Airyscan imaging. While uniformly distributed along the mitochondrial network in control cells (Fig. 6, E and G), CPOX showed mosaic distribution in ~100% Acn-treated cells (Fig. 6, F and G). In these cells, high CPOX localized to the mitochondria with high-cytochrome *c* (Fig. 6, F and G). As was the case for cytochrome *c* distribution (Fig. 2 A; and Fig. S4, H and K), the reduced MTF-induced mosaic distribution of CPOX was

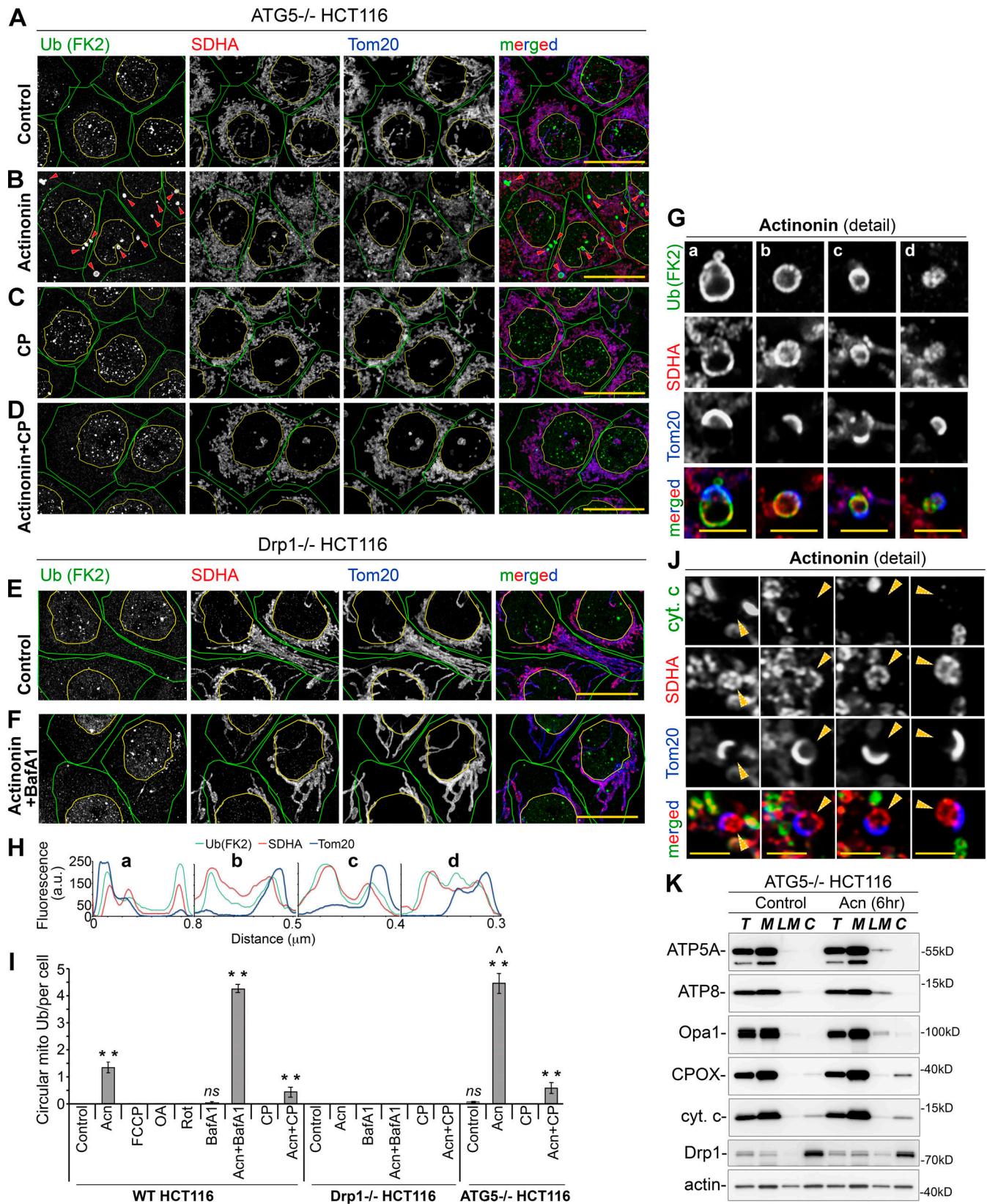


Figure 4. Drp1 and mitochondrial translation are required for the OMM severing and mitochondrial ubiquitination in Acn-treated cells. (A–F) ATG5^{-/-} (A–D), Drp1^{-/-} (E and F), and WT (G) HCT116 cells treated with Acn alone (B and G), CP (C), Acn plus CP (D), Acn plus BafA1 (F), and DMSO (vehicle, A and E) for 6 h were immunolabeled to detect conjugated Ub (FK2 antibody; green), SDHA (red), and Tom20 (blue). In A–F, cells are traced with green lines and nuclei with yellow lines. Red arrowheads indicate examples of mitochondria-associated circular Ub. **(G)** High magnifications of the mitochondria-associated Ub (green), OMM (Tom20; blue), and IMM/matrix (SDHA; red) from Acn-treated WT HCT116 cells are shown. **(H)** Fluorescence intensity linescans along mitochondria

shown in G. Scale bars represent 20 μm in A–F and 1 μm in G. **(I)** Quantification of circular mitochondrial ubiquitination in WT, Drp1^{-/-}, and ATG5^{-/-} HCT116 cells treated as indicated in the figure. Data are represented as mean \pm SD; $n = 3\text{--}6$ ($n = 70$ cells per experiment). **, $P < 0.01$ versus control in WT HCT116 cells; ^, $P < 0.01$ versus Acn in WT HCT116 cells; ns indicates nonsignificant; one-way ANOVA with Bonferroni correction ($\alpha = 0.05$). **(J)** Typical examples of mitochondria with discontinuous OMM from WT HCT116 cells treated with Acn for 6 h and labeled to detect cytochrome c (cyt.c; green), SDHA (red), and Tom20 (blue) are shown. Yellow arrowheads indicate SDHA-positive, cytochrome c-negative mitochondria. Bars represent 1 μm . **(K)** Control and Acn-treated ATG5^{-/-} HCT116 cells were subjected to cell fractionation and Western blot as indicated in the figure. Actin was used as a loading control. C, cytosol; LM, post-mitochondrial LM fractions; M, mitochondria-enriched HM fractions; T, total cell lysate.

inhibited by CP (Fig. 6 G) and Drp1 knockout (Figs. 6 G and S6 H). Mosaic distribution of CPOX was also detectable in Acn-treated HeLa cells (Fig. S6 J), even though expression of this protein in HeLa cells was several fold lower than in HCT116 cells (Fig. S6 K). Localization of TRAP1 in Acn-treated cells was more uniform, with some mitochondria showing increased TRAP1 levels. A subset of mitochondria with high-cytochrome c signal also contained increased TRAP1 fluorescence (Fig. S6 F). Since other mitochondrial markers we tested, including ATP6, ATP8, ClpP, Hsp60, SDHA, SDHB, NDUFB8, and many others (not depicted), showed uniform distribution in control and Acn-treated cells, increased levels of TRAP1 in some mitochondria colocalizing with high-cytochrome c mitochondria is noteworthy.

Reduced MTF induces recruitment of autophagy adaptors p62 and OPT and autophagosomes to the ubiquitinated IMM

Formation of lipidated LC3II (Fig. 2, M and P), degradation of p62 (Fig. 2, L and O), and mitochondrial association of ubiquitinated p62 in Acn-treated cells (Fig. 6 A) suggest that ubiquitination of the IMM proteins may trigger Ub-dependent mitophagy. We investigated if autophagy factors localize to the OMM-severed mitochondria displaying circular IMM ubiquitination. We found that the autophagy adaptor proteins p62 and optineurin (OPT) colocalized with Ub in Acn-treated (Fig. 7 A) or Acn plus BafA1-cotreated (Fig. 7, B and D) WT HCT116 cells and Acn-treated ATG5^{-/-} HCT116 cells (Fig. 7, C and E). Supporting the possibility that ubiquitinated IMM provides the signal for recruiting the autophagy adaptors, the distance between the fluorescence peaks of p62 and OPT relative to the fluorescence peaks of Ub were $0.01 \pm 0.04 \mu\text{m}$ and $-0.01 \pm 0.03 \mu\text{m}$, respectively (Fig. 7 J). While p62 localized to the ubiquitinated IMM in Acn-treated WT and ATG5^{-/-} cells, the autophagosome marker LC3 colocalized with ubiquitinated IMM in Acn- and Acn plus BafA1-treated WT cells (Fig. 7, F, G, and I), but not in Acn-treated ATG5^{-/-} cells (Fig. 7, H and I). Thus, reduced MTF induces ATG5-dependent selective autophagy of ubiquitinated IMM proteins. Furthermore, this finding suggests that autophagy-specific ATG5-ATG12, but not ATG3-ATG12 conjugates that were reported to control mitochondrial homeostasis (Radoshevich et al., 2010), are critical for mitophagy in cells with reduced MTF. Of note, all p62-positive mitochondria with discontinuous Tom20 staining were deficient in cytochrome c (Fig. 7 K), further demonstrating that severing of the OMM is linked to IMM ubiquitination.

Role of Parkin in mosaic distribution of cytochrome c and mitochondrial ubiquitination in cells with reduced MTF

Circular ubiquitination of mitochondria with severed OMM was apparent in HeLa cells (Fig. S6, C and D). Formation of mosaic

cytochrome c/CPOX mitochondria also occurred in these cells (Figs. 1 G and S1 D). Since HeLa cells do not express Parkin (Fig. S6 E; Burman et al., 2017), it is likely that Parkin activity is not required for mitochondrial changes induced by reduced MTF.

The majority of published studies on mitochondrial ubiquitination and mitophagy employed cells expressing exogenous Parkin. As shown in Fig. 8 A, we investigated the effect of ectopic expression of Parkin on mosaic cytochrome c distribution in the model of reduced MTF. This was performed in HeLa cells cotransfected with mCherry-tagged Parkin (Parkin-mCherry) and cyt. c-GFP (Fig. 8 A). The data show that in Acn-treated cells, Parkin-mCherry preferentially associates with the high-cytochrome c mitochondria, especially in the early phase of their formation (Fig. 8 A and Video 8). Acn-treated Parkin-mCherry expressing cells exhibited a significantly reduced number of high cyt. c-GFP mitochondria per cell detected by time-lapse imaging compared with Parkin-deficient cells (11.4 ± 2.5 versus 5.0 ± 2.1 high cyt. c-GFP mitochondria at 300 min in Acn-treated Parkin-deficient and Parkin-mCherry overexpressing cells, respectively; Fig. 3 D). Thus, the high-cytochrome c mitochondria, are primed for degradation by mitophagy. Regardless of the time of treatment with Acn, Parkin-mCherry circumscribed mitochondria (Fig. 8, A–C and E; and Video 8), similarly to the pattern shown by others to occur in uncoupler-treated cells (Cai et al., 2012; Narendra et al., 2008; Tanaka et al., 2010). Similar localization and colocalization of Parkin-YFP with Ub and Tom20 were also detected in both Acn-treated WT and Drp1^{-/-} HCT116 cells (Fig. 8, B and C). Furthermore, at 6 h of Acn treatment, the number of cells showing mitochondria-associated Parkin-YFP and mitochondrial ubiquitination were similar in WT and Drp1^{-/-} cells (Fig. 8 D), indicating that unlike in cells with no ectopic and little endogenous Parkin expression (Fig. 4 G), ubiquitination of the mitochondria in Parkin-overexpressing cells is not controlled by Drp1. Inhibition of mitochondrial translation with CP abrogated Acn-induced mitochondrial translocation of Parkin in both WT and Drp1^{-/-} cells (Fig. 8 D). The number of high-cytochrome c mitochondria per cell was markedly reduced in Parkin-YFP expressing Acn-treated WT cells (Fig. 8, E and G), but not in Parkin-YFP expressing Acn-treated ATG5^{-/-} cells (Fig. 8, F and G), as compared with Parkin-YFP-negative cells from the same samples.

Thus, reduced MTF triggers mitophagy in both Parkin-expressing and Parkin-deficient HeLa cells or low-level Parkin-expressing HCT116 cells. However, unlike in low-level Parkin-expressing or Parkin-deficient cells (Fig. 4, G and I), OMM severing and IMM ubiquitination were not detected in cells ectopically expressing Parkin. Instead, Parkin-overexpressing cells showed ubiquitination of the OMM (Fig. 8, H and I). Quantification

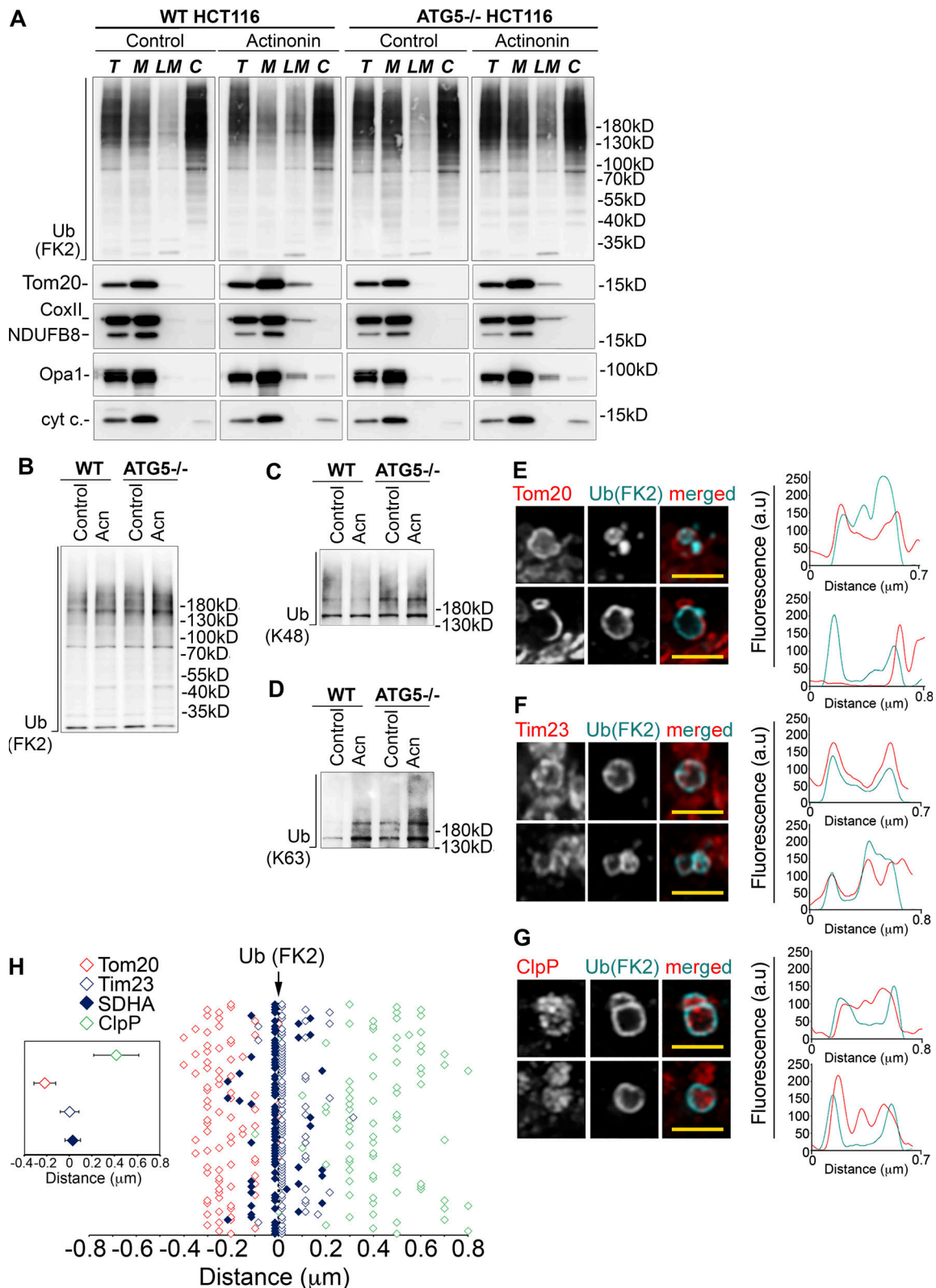


Figure 5. **Mitochondrial ubiquitination in cells with reduced MTF.** (A) WT and ATG5^{-/-} HCT116 cells treated with DMSO (control) or Acn for 6 h were subjected to cell fractionation and Western blot as indicated in the figure. C, cytosol; LM, postmitochondrial LM fractions; M, mitochondria-enriched HM fractions; T, total cell lysate. (B–D) LM fractions from WT and ATG5^{-/-} cells treated with DMSO or Acn for 6 h were analyzed to detect conjugated Ub (FK2); B, K48 Ub chains (C), and K63 Ub chains (D). Similar data were obtained in two independent experiments. (E–G) Single z-section images from Acn-treated WT HCT116 cells. Cells were stained with anti-Ub FK2 mAb (E–G; light blue), anti-Tom20 antibody (OMM; red in E), anti-Tim23 antibody (IMM; red in F), and anti-ClpP antibody (matrix; red in G). Two typical examples for each condition are shown. Fluorescence intensity profiles are shown on the right. Scale bars

represent 1 μm . **(H)** Localization of OMM (Tom20), IMM (Tim23 and SDHA), and matrix (ClpP) markers relative to Ub (FK2) signal. The insert shows mean \pm SD of data shown in the main graph. $n = 60$ per condition pulled from $n = 3\text{--}4$ independent experiments. To facilitate data evaluation, values on the main graph were slightly right-shifted for Tim23 and slightly left-shifted for SDHA.

of the localization of Parkin-YFP and Ub (FK2) fluorescence peaks, relative to markers of different mitochondrial compartments (**Fig. 8 I**), revealed high colocalization between Ub and Parkin (distance between fluorescence peaks, $-0.01 \pm 0.05 \mu\text{m}$) and between Ub and

Tom20 ($-0.01 \pm 0.06 \mu\text{m}$), but not between Ub and Tim23 ($0.21 \pm 0.10 \mu\text{m}$).

Parkin-mediated mitophagy relies on the accumulation of PINK1 on the OMM of dysfunctional mitochondria. PINK1-mediated

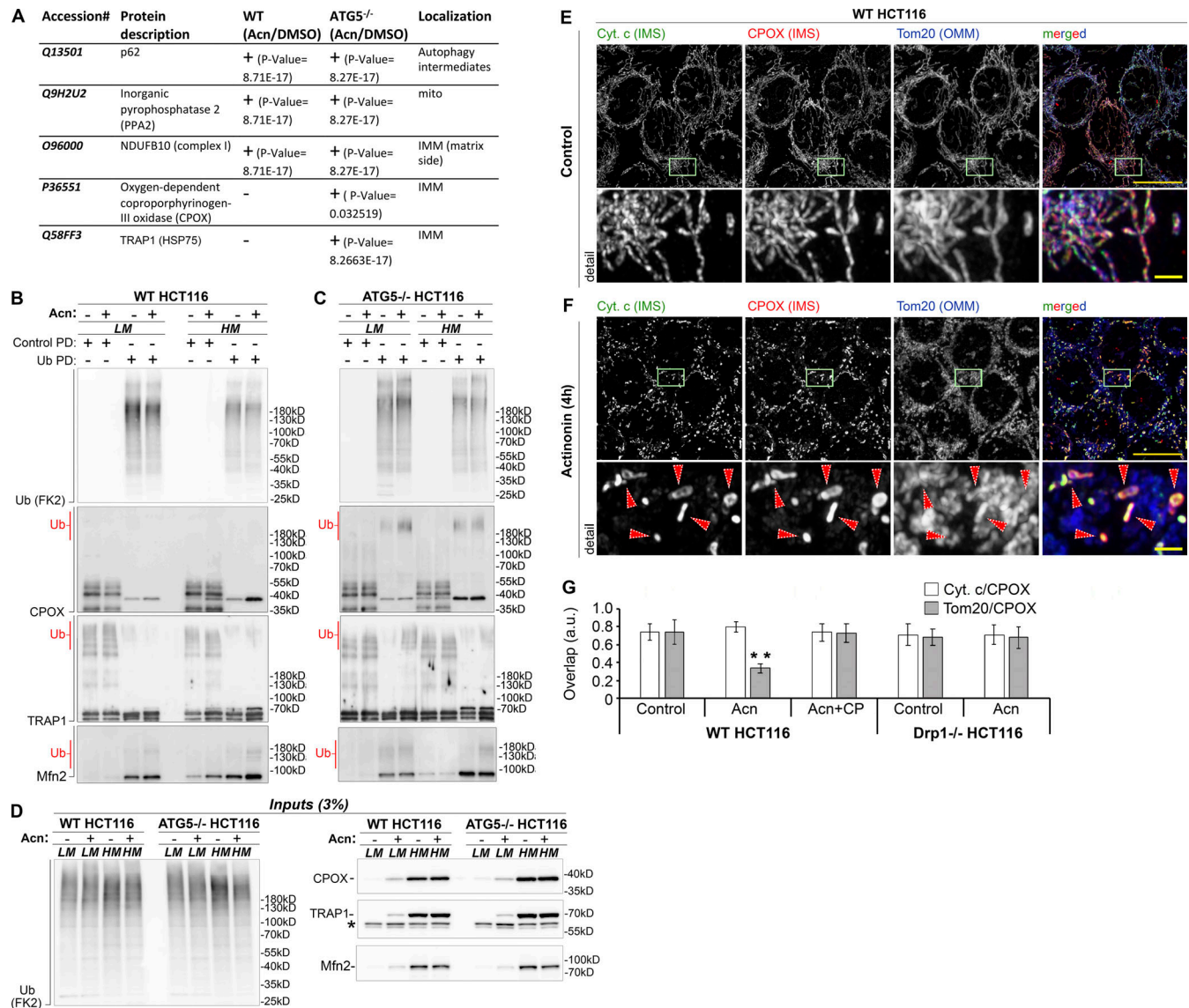


Figure 6. Identification of mitochondrial proteins ubiquitinated in cells with reduced MTF. (A) Summary of mass spectrometry analyses of ubiquitinated proteins enriched in membrane fractions of Acn-treated versus control (DMSO-treated) cells. For the complete dataset, see Data S1. **(B–D)** Mitochondria-enriched HM and LM fractions from DMSO (control)– or Acn-treated WT (B) or ATG5^{-/-} HCT116 (C) cells were subjected to Ub pull-down (PD) under denaturing conditions and analyzed by Western blot as indicated in the figure. Inputs (3% of samples used for the Ub pull-down) are shown in D. High-molecular-weight (apparently ubiquitinated) subsets of CPOX, TRAP1, and Mfn2 are marked with a red “Ub.” Upon stress, Mfn2 is degraded by the UPS (McLelland et al., 2018; Tanaka et al., 2010), and ubiquitination of this protein in Acn-treated cells was used as a reference. **(E and F)** WT HCT116 cells treated with DMSO (control; E) or Acn (F) were labeled to detect cytochrome c (Cyt. c; green), CPOX (red), and Tom20 (blue). Arrowheads in F indicate examples of high-cytochrome c/high-CPOX mitochondria. Detail images are from areas outlined with light green rectangles. Scale bars represent 20 μm (2 μm in detail images). **(G)** Overlap among cytochrome c, CPOX, and Tom20 in control and Acn-treated WT and Drp1^{-/-} and Acn plus CP-treated WT HCT116 cells was estimated from maximum intensity projection images (exemplified in E and F). The values are shown as Pearson’s correlation coefficient. Data are represented as mean \pm SD; $n = 40$ cells per condition. **, $P < 0.01$ versus control in WT HCT116 cells (all other samples were not significant); one-way ANOVA with Bonferroni correction ($\alpha = 0.05$).

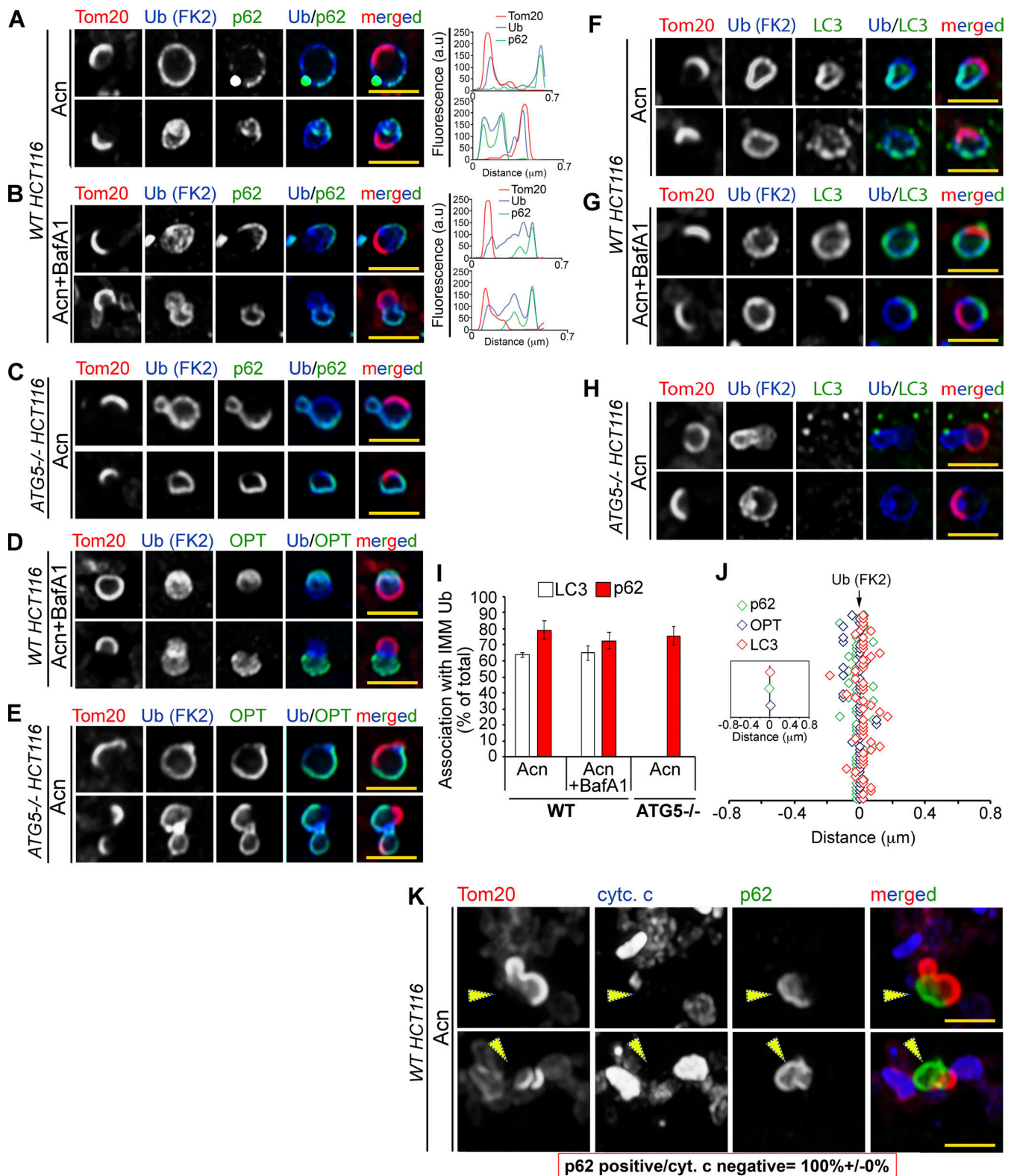


Figure 7. **Recruitment of autophagy proteins to the ubiquitinated IMM in Acn-treated cells.** (A–G) WT (A, B, D, F, and G) and ATG5^{-/-} (C, E, and H) HCT116 cells were treated with Acn (A, C, E, F, and H) or cotreated with Acn and BafA1 (B, D, and G). Cells were labeled with anti-Ub FK2 mAb (blue in A–H), anti-Tom20 antibody (red in A–H), anti-p62 antibody (green in A–C), anti-OPT antibody (OPT; green in D and E), and anti-LC3 antibody (green in F–H). Two typical examples of mitochondria with OMM severing are shown for each condition. Scale bars represent 1 μ m. (I) The localization of p62 and LC3 with circular Ub in cells treated and exemplified in A–C and F–H was blindly quantified. $n = 3$ ($n > 50$ per experiment). (J) Quantification of positions of p62, OPT, and LC3 relative to Ub signal. The insert shows mean \pm SD of data shown in the main graph. $n = 50$ per condition. Data pulled from $n = 3$ independent experiments. Examples of fluorescence intensity profiles used for quantifications are shown on the right of images in A and B. (K) p62-positive mitochondria are deficient in

cytochrome c. Cells treated with Acn for 6 h were immunostained to detect Tom20 (red), cytochrome c (cyt. c; blue), and p62 (green). Typical examples are shown. Arrowheads point to p62-positive/cytochrome c-negative mitochondria. 100% of p62-positive mitochondria are deficient in cytochrome c signal ($n = 2$, $n = 50$ per experiment). Scale bars represent 1 μm .

phosphorylation of Ub conjugated to the OMM proteins is one of the hallmarks of Parkin-mediated mitophagy (Kane et al., 2014; Koyano et al., 2014; Lazarou et al., 2015; Okatsu et al., 2015). We tested mitochondrial accumulation of phosphorylated Ub in Acn-treated Parkin-deficient and Parkin-YFP-expressing cells. The data show colocalization of phospho-Ub and conjugated Ub in YFP-Parkin-expressing cells (Fig. 8 K), but not in untransfected cells (Fig. 8 J). This finding indicates that in Parkin-deficient cells, PINK1-dependent Ub phosphorylation is not required for mitophagy triggered by reduced MTF.

Discussion

Here, we report that cells adapt to mitochondrial proteotoxicity through a Drp1-mediated mechanism that involves the severing of the OMM followed by IMM ubiquitination and autophagic degradation of ubiquitinated IMM proteins. Most published research on mitochondrial ubiquitination and mitophagy investigated these processes after they had been triggered with uncouplers (e.g., CCCP or FCCP) or OXPHOS inhibitors (e.g., OA). These compounds diminish $\Delta\Psi_m$, which is considered a terminal manifestation of mitochondrial dysfunction. To gain insights into events that contribute to mitochondrial ubiquitination and/or mitophagy upstream of $\Delta\Psi_m$ decline, we employed Acn and CP agents that specifically target mitochondrial translation. While CP inhibits translation, Acn reduces the fidelity of mitochondrial translation without reducing its rate (Battersby and Richter, 2013; Richter et al., 2013; Richter et al., 2015). The Acn-induced mitochondrial proteotoxicity model was instrumental in determining the mechanisms of mitochondrial ribosome decay (Richter et al., 2013) and the identification of mitochondrial mitochondrial-AAA (m-AAA) protease subunit AFG3L2-dependent quality control pathway (Richter et al., 2015; Sheth et al., 2014).

As reported by others (Richter et al., 2015; Sheth et al., 2014), we found that cells treated with Acn exhibited a delayed decline in $\Delta\Psi_m$ (Fig. 3 G). However, in contrast to these earlier studies, our imaging experiments revealed that the $\Delta\Psi_m$ decline was mostly restricted to a subset of the mitochondria showing abnormal accumulation of IMM/IMS proteins cytochrome c and CPOX, a protein implicated in heme synthesis (Ausenda et al., 2009; mosaic mitochondria). Formation of mosaic mitochondria are detected in cells expressing low levels of Parkin or deficient in Parkin expression and are followed by three events that appear to be successive: (1) OMM severing, (2) IMM ubiquitination, and (3) assembly of autophagy adaptors and autophagosomes on ubiquitinated IMM. Ectopic expression of Parkin reduced the accumulation of mosaic mitochondria, likely due to their preferential targeting and degradation by Parkin-mediated mitophagy. We propose that mosaic mitochondria are mitophagy intermediates in both Parkin-deficient and Parkin-expressing cells. Furthermore, instead of the OMM severing and IMM

ubiquitination observed in the absence of Parkin, the canonical translocation of Parkin to the OMM and OMM ubiquitination was detected in Acn-treated Parkin-expressing cells.

Reduced MTF leads to a mosaic distribution of cytochrome c and CPOX in WT cells, but not in cells in which the mitochondrial fission factor Drp1 was ablated. Furthermore, Mff and MiD51, primary mitochondrial receptors of Drp1 (Gandre-Babbe and van der Bliiek, 2008; Palmer et al., 2013), are also required for this process. These findings indicate that reduced MTF may result in remodeling of mitochondrial membranes, leading to asymmetrical localization of cytochrome c and CPOX. The requirement for Drp1, Mff, and MiD51 in this process suggests that asymmetrical mitochondrial fission may be necessary to produce a mixture of “high” and “low” cytochrome c mitochondria within the cell, resembling Drp1-mediated separation of low- $\Delta\Psi_m$ mitochondria during homeostatic, Parkin-dependent mitophagy in untreated β cells (Twig et al., 2008) and HeLa (Cho et al., 2019) cells, as well as separation of mitochondrial matrix proteins in the stationary phase of mitophagy in yeast (Abeliovich et al., 2013). Functional and morphological heterogeneity of mitochondria within individual cells, including heterogeneity in $\Delta\Psi_m$, response to calcium signals, resistance to apoptosis, and oxidative stress, has been shown (Collins et al., 2002; Kuznetsov and Margreiter, 2009). However, the mosaic distribution of mitochondrial proteins in distinct mitochondria within a cell, as exemplified here by cytochrome c and CPOX, has not been reported (to our knowledge).

What could be the mechanisms that are responsible for establishing the mosaic distribution of these proteins? The submitochondrial localization of cytochrome c depends on mitochondrial cristae organization (Scorrano et al., 2002) and/or cardiolipin distribution along the IMM (Ott et al., 2007). The IMM-localized OXPHOS complexes can affect cristae abundance and/or structure (Cogliati et al., 2016) and cardiolipin levels and/or localization (Paradies et al., 2014). Protein contacts of an indirect or direct nature would be a way to generate cytochrome c and CPOX sequestration in some mitochondria. In this scenario, abnormal accumulation of OXPHOS complexes apparent in Acn-treated cells could locally increase the abundance of IMM-binding IMS proteins, such as cytochrome c and CPOX, interacting with these complexes. The physiological status of the mitochondria affects the distribution of mitochondrial proteins between different subdomains (Vogel et al., 2006). A similar (but larger in scale) redistribution could lead to major changes in cytochrome c and CPOX, as we show here in a model of mitochondrial proteotoxicity. As proposed by Twig et al. (2008), the mitochondrial fission-fusion cycle would lead to further accumulation of degradative cargo within some mitochondria, early in the process, followed by Drp1-mediated separation of mitochondria with highly uneven levels of cytochrome c (and possibly the OXPHOS complexes), late in the process. Since most cytochrome c is sequestered within mitochondrial cristae

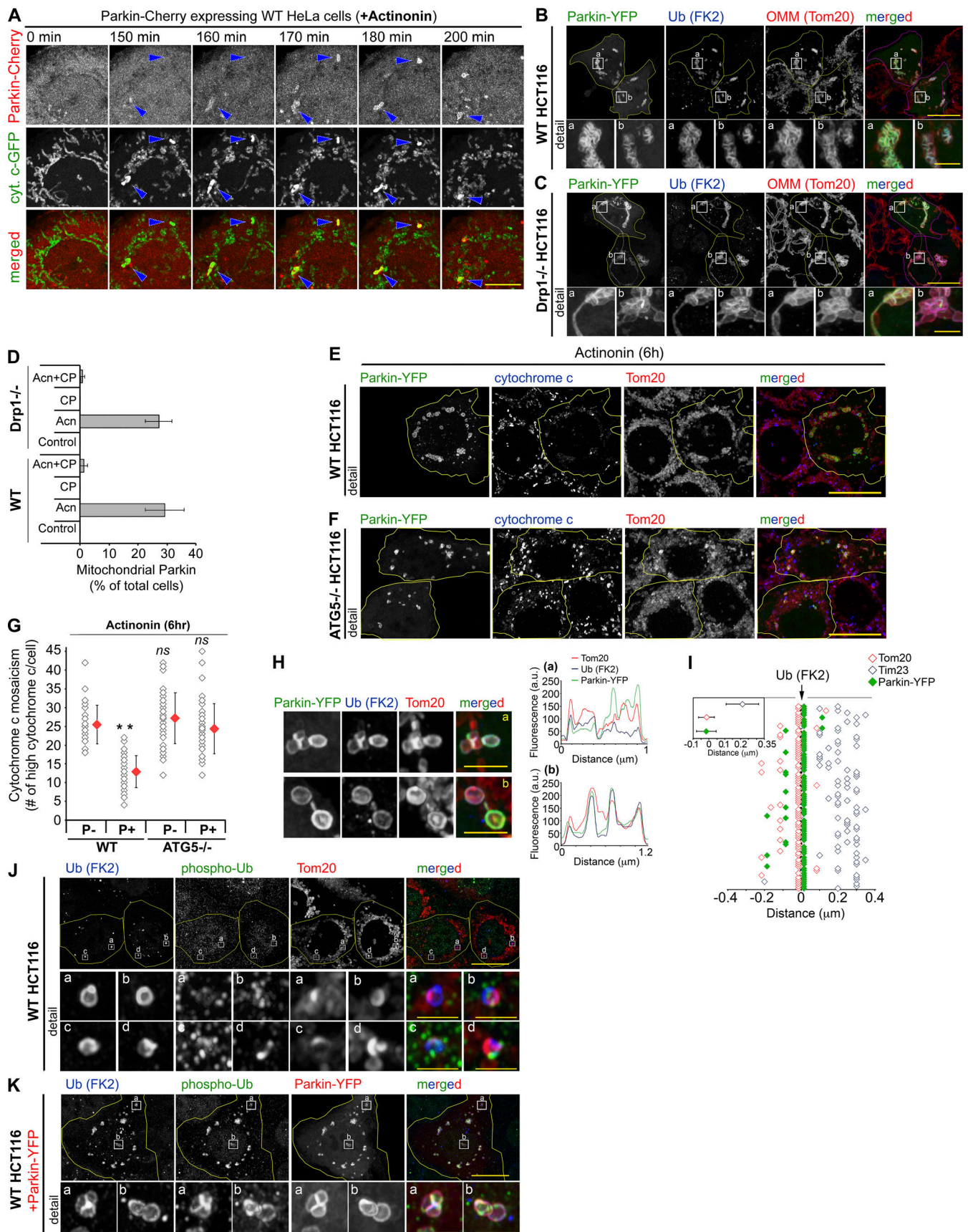


Figure 8. **Effects of reduced MTF in Parkin-overexpressing WT and Drp1^{-/-} cells.** (A) WT HeLa cells cotransfected with cyt. c-GFP (green) and Parkin-Cherry (red) were treated with Acn and subjected to time-lapse live-cell imaging. Arrowheads indicate high-cyt. c-GFP mitochondria and the corresponding

Parkin-Cherry. Scale bar represents 10 μm . **(B and C)** WT (B) and Drp1^{-/-} (C) HCT116 cells transfected with Parkin-YFP (green in B and C), followed by treatment with Acn for 6 h, and immunostaining to detect conjugated Ub (FK2; blue) and Tom20 (red). Detail images in B and C are from areas outlined with rectangles. Scale bars represent 20 μm (5 μm in detail images). **(D)** Parkin-YFP-expressing WT and Drp1^{-/-} cells treated with DMSO (control), Acn, CP, and Acn plus CP for 6 h were quantified for mitochondrial localization of Parkin. Parkin-YFP-expressing cells were counted. Data represent mean \pm SD; $n = 5$ ($n = 100$). **(E and F)** WT (E) and ATG5^{-/-} (F) HCT116 cells transfected with Parkin-YFP (green) were treated with Acn for 6 h and immunostained to detect cytochrome c (blue) and Tom20 (red). Parkin-YFP-expressing cells are traced with yellow lines. Scale bars represent 20 μm . **(G)** Number of high-cytochrome c mitochondria per cell was blindly quantified in Parkin-YFP (P+)-expressing (P+) and deficient (P-) WT and ATG5^{-/-} cells treated with Acn. P+ and P- cells were from the same samples. $n = 50$ cells/condition. **, $P < 0.01$ versus WT P-; ns indicates nonsignificant; one-way ANOVA with Bonferroni correction ($\alpha = 0.05$). **(H)** Submitochondrial localization of Parkin-YFP (green) and Ub (blue) in Acn-treated cells. Scale bars represent 5 μm . **(I)** Quantification of relative position of OMM (Tom20), IMM (Tim23), and Parkin-YFP versus the Ub (FK2) signal. $n = 60$ per condition. Data pulled from $n = 3$ independent experiments. To facilitate data evaluation, the values were slightly right-shifted for Parkin-YFP and slightly left-shifted for Tom20. **(J and K)** Untransfected (J) and Parkin-YFP transfected (K) WT HCT116 cells were treated with Acn for 6 h, followed by immunostaining to detect Ub (FK2; blue in merged images) and phosphorylated Ub (phosphor-Ub; green in merged images). YFP-Parkin is pseudocolored in red (K). Detail images in J and K are from areas marked with rectangles from cells overlaid with yellow lines. Scale bars represent 20 μm (2 μm in detail images).

(Cogliati et al., 2016; Scorrano et al., 2002), another possibility is that reduced MTF could cause the formation of mitochondrial subsets dramatically varying in cristae density. In this scenario, high-cytochrome c mitochondria would correspond to mitochondria with abnormally dense cristae structures. Given the role of OXPHOS complexes in the control of mitochondrial cristae structure and abundance (Cogliati et al., 2016; Zick et al., 2009), both mechanisms proposed above may contribute to the mosaic distribution of cytochrome c and CPOX. Nevertheless, the high-cytochrome c/CPOX mitochondria contain information priming them for mitophagy-mediated degradation. Notably, CPOX, the protein showing mosaic distribution, is also ubiquitinated in light mitochondria from Acn-treated cells. Thus, it is plausible that ubiquitination of CPOX and likely other IMM-associated IMS proteins serves as a signal recruiting mitophagy factors to the mitochondria with severed OMM, connecting mosaic mitochondrial distribution and mitophagy.

In contrast to most mitochondria in Acn-treated cells, which show relatively normal $\Delta\Psi_m$, the high-cytochrome c mitochondria display vastly reduced $\Delta\Psi_m$. It is likely that in cells that express Parkin, Parkin translocation to these organelles is due to reduced $\Delta\Psi_m$, trapping of PINK1 on the OMM and subsequent Ub phosphorylation, which are the hallmarks of Parkin/PINK1-mediated mitophagy (Karbowski and Youle, 2011; Lazarou et al., 2015; Narendra et al., 2008). In contrast, the accumulation of high-cytochrome c mitochondria in Parkin-deficient cells is followed by OMM severing and IMM ubiquitination, without phosphorylated Ub accumulation. OMM severing and IMM ubiquitination could serve as a failproof pathway in cells expressing low levels of Parkin or when the Parkin/PINK1 pathway is dysfunctional.

What could be the mechanism by which high-cytochrome c mitochondria are targeted for degradation in Parkin-deficient cells? The data suggest a model in which IMM exposure to the cytosol, apparent in mitochondria with severed OMM, allows cytosolic components of the UPS to access the IMM. Under normal growth conditions, IMM proteins are separated from the cytosol by the OMM or by chaperone proteins during their import into the mitochondria. We propose that cytosol-exposed IMM contains clues, such as CPOX, recognized by cellular surveillance systems as “unfamiliar”, and thereby subjected to degradation in a process similar to xenophagy (the autophagy mode targeting intracellular microorganisms). Indeed, bacteria

escaping from phagosomes into the cytosol are ubiquitinated (Manzanillo et al., 2013) and thereby targeted for degradation by xenophagy. IMM ubiquitination and the fact that p62 and OPT, which also mediate xenophagy (Zheng et al., 2009), accumulate on ubiquitinated IMM support the possibility that a similar process participates in the degradation of IMM-ubiquitinated mitochondrial fragments. Since the number of mitochondria showing OMM severing and IMM ubiquitination significantly increases in cells cotreated with Acn and the autophagy inhibitor BafA1 or Acn-treated autophagy-deficient ATG5^{-/-} cells, the possibility that cytosol-exposed IMM serves as an autophagy-priming signal, similarly to bacterial membranes in xenophagy, is likely. Despite this model’s speculative nature, we suggest that it provides a useful platform for further investigation.

The process reported here could be the mammalian equivalent of a mitochondrial quality control mechanism reported in yeast (Hughes et al., 2016). Hughes et al. found that the selective elimination of mitochondrial proteins in aged yeast includes their sorting into mitochondria-derived compartments. Like the Acn-induced OMM severing and IMM ubiquitination shown here, degradation of mitochondria-derived compartments required mitochondrial fission but was not directly triggered by $\Delta\Psi_m$ decline (Hughes et al., 2016).

Mitochondrial translation defects and mtDNA mutations causing abnormal mitochondrial protein expression are linked to many diseases, including neurodegeneration and some mtDNA mutation-associated pathologies (Battersby and Richter, 2013; Richter et al., 2013; Richter et al., 2015; Sheth et al., 2014; Smits et al., 2010). We believe that in addition to revealing a novel mitochondrial quality control mechanism in model cells, our findings shed light on how mitochondrial proteotoxicity may contribute to aging and disease. Furthermore, considering that cancer cells either express extremely low levels of Parkin or do not express this protein at all (Burman et al., 2017; Villa et al., 2017), our work also provides a new perspective on the regulation of mitophagy in transformed cells.

Materials and methods

Cells and cell culture

HCT116 cells were maintained in McCoy’s 5A medium (Thermo Fisher Scientific) supplemented with 10% FBS (Thermo Fisher

Scientific), nonessential amino acids (Thermo Fisher Scientific), sodium pyruvate (Thermo Fisher Scientific), and penicillin/streptomycin (Thermo Fisher Scientific). HeLa cells and MEFs were maintained in DMEM (Thermo Fisher Scientific) supplemented as McCoy's 5A medium. MEFs were provided by Dr. Mike Ryan (Monash University, Melbourne, Australia) and were described in (Osellame et al., 2016). M17 neuroblastoma cells were provided by Dr. Richard J. Youle (National Institutes of Health, Bethesda, MD). M17 cells were maintained in Opti-MEM (Thermo Fisher Scientific) supplemented with 10% FBS and 2 mM glutamine. HCT116, HeLa, and M17 cells were originally acquired from the ATCC. Cell lines used for determination of Parkin expression by Western blot were provided by Dr. Shengyun Fang (University of Maryland, Baltimore, MD). Cells were maintained in 5% CO₂ at 37°C.

Reagents

Acn (Enzo Life Sciences or Cayman Chemicals) was used at 200 μM, FCCP (Enzo Life Sciences) was used at 20 μM; BafA1 (Cell Signaling Technology) was used at 100 nM; CP (Sigma-Aldrich) was used at 200 μM; rotenone (Sigma-Aldrich) was used at 50 μM; the mixture of oligomycin (Sigma-Aldrich) and antimycin A (OA; Sigma-Aldrich) was used at 10 μg/ml and 5 μg/ml, respectively; ABT-737 (Axxora) was used at 10 μM; and TMRM (Thermo Fisher Scientific) was used at 50 nM.

Knockout cells, mtDNA depletion, DNA constructs, and transfections

Drp1^{-/-}, Mff^{-/-} HCT116 and Mff^{-/-} and Drp1^{-/-} HeLa cells were reported previously (Cherok et al., 2017), Bax^{-/-}/Bak^{-/-} DKO and ATG5^{-/-} HCT 116 cells were provided by Dr. Richard J. Youle (National Institutes of Health). They were described previously (Burman et al., 2017; Wang and Youle, 2012). Mammalian expression vectors encoding MYC-tagged dominant-negative mutant of Drp1 (MYC-Drp1^{K38A}), mitochondrial matrix-targeted RED fluorescent protein (mito-RFP) were reported before (Karbowski et al., 2002). Cytochrome c-GFP was a gift from Douglas Green (St. Jude Children's Research Hospital, Memphis, TN; Addgene; plasmid no. 41182; <http://n2t.net/addgene:41182>; RRID:Addgene_41182; Goldstein et al., 2000). Drp1-mCherry was a gift from Gia Voeltz (University of Colorado Boulder, Boulder, CO; Addgene plasmid no. 49152; <http://n2t.net/addgene:49152>; RRID:Addgene_49152; Friedman et al., 2011). Parkin-YFP and Parkin-mCherry were provided by Dr. R J Youle (National Institutes of Health, Bethesda, MD; Burman et al., 2017; Tanaka et al., 2010). The mammalian expression vector of human NDUFA12 protein (also known as a DAPI3) with a HA-tag at the C terminus were provided by Dr. N Yadava (University of Maryland, Baltimore, MD). Cells were transfected with Lipofectamine 3000 (Thermo Fisher Scientific), according to the manufacturer's instructions. Cells were used at ~16–36 h after transfection. For mtDNA depletion, HCT116 cells were treated with 50 ng/ml ethidium bromide (Sigma-Aldrich) for ~2 mo and then maintained in cell culture media supplemented with 10 ng/ml of ethidium bromide (Spadafora et al., 2016). Media containing ethidium bromide were replaced every 3 d. mtDNA depletion

was verified by Western blot for mtDNA-encoded mitochondrial proteins.

Cell lysates, cell fractionation, and Western blot

For total cell lysates, cells were collected by scrapping into ice-cold PBS, and cells were then washed and suspended in ice-cold PBS. Cell suspensions (100–200 μl) were lysed in the same volumes of 2 × SDS sample buffer (Thermo Fisher Scientific) supplemented with 5% β-mercaptoethanol (Millipore) and incubated at 100°C for 10 min, as described elsewhere (Cherok et al., 2017; Xu et al., 2016). For rat tissue cell lysates, freshly excised tissues obtained from young adult male Sprague Dawley rats were homogenized in ice-cold PBS (supplemented with protease inhibitors; Sigma-Aldrich), followed by centrifugation at 500×g for 5 min to remove tissue debris. The supernatants were centrifuged at 2,500×g at 4°C for 10 min. Supernatants were removed, and pellets were suspended in ice-cold PBS supplemented with protease inhibitors. The subsequent steps were as in the above-described total cell lysate preparation. Mitochondria-enriched HM fractions and LM fractions were generated as previously described (Cherok et al., 2017; Xu et al., 2016). Briefly, cells were washed once with ice-cold PBS and scraped into 15-ml tubes in ice-cold PBS; this was followed by centrifugation at 500×g for 5 min. The cell pellets were re-suspended in ~3 vol fractionation buffer (10 mM Hepes, 10 mM NaCl, 1.5 mM MgCl₂, and protease inhibitors [Sigma-Aldrich]). Cells were then passed 15 times through a 25-G needle attached to a 1-ml syringe to disrupt cell membranes. This suspension was centrifuged at 2,500×g at 4°C for 5 min to remove unbroken cells and cell debris. The supernatant was centrifuged at 6,000×g at 4°C for 10 min to pellet the HM fraction. To reduce cytosolic contamination, HM fractions were washed with ice-cold PBS supplemented with protease inhibitors (Roche) and 5 mM N-ethylmaleimide and recentrifuged at 6,000×g at 4°C for 10 min. Post-HM supernatants were centrifuged at 21,000×g at 4°C for 60 min. Supernatants were removed and used as cytosolic fractions. LM-enriched pellets were washed with ice-cold PBS supplemented with protease inhibitors (Roche) and 5 mM N-ethylmaleimide and recentrifuged at 21,000×g at 4°C for 60 min. Protein concentrations were measured directly in the SDS-PAGE samples using a NanoDrop 1000 spectrophotometer (Thermo Fisher Scientific). Proteins were separated on 4–20% gradient Novex Tris-glycine polyacrylamide gels (Thermo Fisher Scientific) and transferred onto polyvinylidene fluoride membranes (Bio-Rad Laboratories). Membranes were blocked in either 1% BSA (detection of Ub) or 5% blocking-grade nonfat dry milk (Bio-Rad Laboratories; other antibodies) in PBS-Tween20 and incubated with primary antibodies overnight at 4°C, followed by horseradish peroxidase-conjugated anti-mouse (Cell Signaling Technology; catalog no. CST-7076) or anti-rabbit (Cell Signaling Technology; catalog no. CST-7074) secondary antibodies for 60 min at RT. Blots were developed with Super Signal West Pico ECL (Thermo Fisher Scientific). The more sensitive, Super Signal West Femto ECL (Thermo Fisher Scientific) reagent was used to detect endogenous Parkin. Blots were imaged using Amersham Imager 600 chemiluminescence imager (GE Healthcare Life Sciences). Antibodies used for Western blotting

were anti-Tom20 polyclonal antibody (Proteintech, 1:10,000; catalog no. PTG-11802-AP), anti-Tom40 polyclonal antibody (Proteintech, 1:10,000; catalog no. PTG-18409-AP), anti-Ub FK2 mAb (Sigma/Millipore, 1:2,000; catalog no. SIG-04-263), anti-Ub mAb (Santa Cruz Biotechnology; clone P4D1, 1:5,000; catalog no. sc-8017), anti-Ub K48 chain rabbit mAb antibody (Sigma/Millipore; clone Apu2, 1:2,000; catalog no. SIG-05-1307), anti-Ub K63 chain rabbit mAb (Sigma/Millipore; clone Apu3, 1:1,000; catalog no. SIG-05-1308), anti-ATP5a1 polyclonal antibody (Proteintech; 1:5,000; catalog no. PTG-14676-1-AP), anti-ATP6 polyclonal antibody (Proteintech; 1:2,000; catalog no. PTG-55313-1-AP), anti-ATP8 polyclonal antibody (Proteintech; 1:2,000; catalog no. PTG-26723-1-AP), anti-CPOX polyclonal antibody (Proteintech; 1:5,000; catalog no. PTG-12211-1-AP), anti-TRAP1 polyclonal antibody (Proteintech; 1:10,000; catalog no. PTG-10325-1-AP), anti-human OXPHOS mAb cocktail (Abcam; 1:2,000; catalog no. ab110411), anti-p62/SQTS polyclonal antibody (Proteintech; 1:10,000; catalog no. PTG-18420-1-AP), anti-LC3 polyclonal antibody (Proteintech; 1:2,000; catalog no. PTG-14600-1-AP), anti-Opa1 mAb (BD Biosciences; 1:2,000; catalog no. PMG-623606), anti-Mfn2 rabbit mAb (Cell Signaling Technology; clone d2d10; 1:2,500; catalog no. CST-9482), anti-Drp1 mAb (BD Biosciences; 1:2,000; catalog no. PMG-611113), anti-Parkin mAb (Cell Signaling Technology; 1:2,000; catalog no. CST-4211), anti-Bax polyclonal antibody (Proteintech; 1:2,000; catalog no. PTG-50599-2-Ig), anti-Bak polyclonal antibody (Sigma-Aldrich; 1:1,000; catalog no. SIG-ABC12), anti-Caspase 1 rabbit mAb (Cell Signaling Technology; 1:2,500; catalog no. CST-2225S), anti-caspase 9 rabbit mAb (Cell Signaling Technology; clone C9; 1:2,000; catalog no. CST-9508), anti-PARP polyclonal antibody (Proteintech; 1:2,000; catalog no. PTG-13371-1-AP), anti- β -actin polyclonal antibody (Cell Signaling Technology; 1–10,000; catalog no. CST-4967S), and anti-HA-tag mAb (Invitrogen; 1:5,000; catalog no. 26183). Densitometric evaluations of protein expression was performed using the ImageJ image analysis software (National Institutes of Health), as reported previously (Cherok et al., 2017; Xu et al., 2016).

Isolation of ubiquitinated proteins

HM and LM fractions were solubilized in denaturing buffer (1% SDS, 5 mM EDTA, and 10 mM β -mercaptoethanol). Samples were incubated at 100°C for 10 min, centrifuged to remove unsolubilized material, and diluted 10 times with ice-cold immunoprecipitation buffer (20 mM Tris-HCl, pH 7.5, 150 mM NaCl, 1 mM EDTA, 0.5% NP-40, 5 mM N-ethylmaleimide, and protease inhibitors). Ubiquitinated proteins were isolated using UBIQAPTURE-Q kit (Enzo Life Sciences), as described by the manufacturer. Protein A/G agarose beads (Invitrogen) were used as control.

Immunofluorescence

Immunofluorescence was performed as previously described (Cherok et al., 2017; Xu et al., 2011). Briefly, cells grown in two- or four-well chamber slides (Lab-Tek; model 1 German borosilicate; VWR) were fixed with freshly prepared 4% formaldehyde in PBS solution (Thermo Fisher Scientific; using 16% methanol-free formaldehyde) for 20 min at RT and then permeabilized

with permeabilization buffer (PB; 0.15% Triton X-100 in PBS) for 20 min at RT. After blocking with blocking buffer (BB; PB supplemented with 7.5% BSA) for 45 min, samples were incubated with primary antibodies suspended in BB for 90 min at RT, followed by three washes with BB and incubation with secondary antibodies diluted in BB for 60 min at RT. Primary antibodies used were anti-Tom20 polyclonal antibody (Proteintech; 1:1,000; catalog no. PTG-11802-AP), anti-Tim23 polyclonal antibody (Proteintech; 1:100; catalog no. PTG-11123-1-AP), anti-cytochrome c mAb (BD Biosciences; 1:1,000; catalog no. PMG-556432), anti-ClpP polyclonal antibody (Proteintech; 1:200; catalog no. PTG-15698-1-AP), anti-SDHA polyclonal antibody (Proteintech; 1:250; catalog no. PTG-14865-1-AP), anti-p62 polyclonal antibody (Proteintech; 1:500; catalog no. PTG-18420-1-AP), anti-OPT polyclonal antibody (Proteintech; 1:500; catalog no. PTG-10837-AP), anti-LC3 polyclonal antibody (Proteintech; 1:500; catalog no. PTG-14600-1-AP), anti-CPOX polyclonal antibody (Proteintech; 1:500; catalog no. PTG-12211-1-AP), anti-TRAP1 polyclonal antibody (Proteintech; 1:500; catalog no. PTG-10325-1-AP), and anti-Ub FK2 mAb (Sigma/Millipore; 1:2,000; catalog no. SIG-04-263). Secondary antibodies were highly cross-absorbed goat anti-mouse Alexa Fluor 488 (Thermo Fisher Scientific; 1:1,000; catalog no. INV-A11029) and goat anti-rabbit Alexa Fluor 568 (Thermo Fisher Scientific; 1:1,000; catalog no. INV-A11036). In triple-labeling experiments, cells were immunostained as above, followed by three washes with BB and incubation with anti-Tom20 antibodies conjugated with Alexa Fluor 647 fluorophore (Santa Cruz Biotechnology; 1:100; catalog no. sc-17764 AF647) for 90 min at RT. After three washes with PBS, cells were subjected to Airyscan imaging. Immunolabeled cells were stored in PBS at 4°C and imaged within 10 d after processing.

Image acquisition

Images were acquired with a Zeiss LSM 880 confocal microscope (Zeiss MicroImaging) equipped with an Airyscan super-resolution imaging module using a 63/1.40 Plan-Apochromat Oil differential interference contrast M27 objective lens (Zeiss MicroImaging), as described previously (Cherok et al., 2017; Xu et al., 2016). The 488-nm argon laser line, 561-nm diode-pumped solid-state laser (DPSS) 561 laser and 633-nm HeNe 633 laser were used to detect Alexa Fluor 488, Alexa Fluor 546, and Alexa Fluor 647, respectively. The z-stacks covering the entire depth of cells with intervals of 0.18 μ m were acquired, followed by Airyscan image processing (set at 6), and, in some cases, generation of maximum intensity projection images. The lateral resolution of resulting images was \sim 120 nm.

Time-lapse live-cell imaging

For time-lapse imaging, cells were grown on 4-well chamber slides (Lab-Tek; model 1 German borosilicate; VWR) to 30–50% confluency. Cells were transfected with respective mammalian expression vectors <30 h before analyses. In all time-lapse experiments, chamber slides were mounted on the environmental control chamber (Stagetop TIZW Series, Neco Incubation System with sensor feedback system) attached to Zeiss LSM 880 confocal microscope (Zeiss MicroImaging) set at 5% CO₂ and

37°C and imaged in imaging medium (Phenol Red-free DMEM supplemented with 10% FBS (Thermo Fisher Scientific), non-essential amino acids (Thermo Fisher Scientific), sodium pyruvate (Thermo Fisher Scientific), and penicillin/streptomycin (Thermo Fisher Scientific). For $\Delta\Psi_m$ imaging, cells were loaded with 50 nM TMRM (Thermo Fisher Scientific) dissolved in imaging medium for 45 min followed by drug treatment. Imaging was initiated at ~60 min after TMRM addition. The 561-nm DPSS 561 laser used to detect TMRM was set at 0.06% in all time-lapse experiments. In all time-lapse experiments, five z-sections with the interval of 0.3 μm between each section, resulting in 1.2 μm depth, were acquired for each time point.

Image analysis and processing

All image processing and analyses were done using ZEN image acquisition and processing software (Zeiss MicroImaging; version 2.3SPL). Colocalization/overlap between cytochrome c (marker of the IMS) and ClpP (mitochondrial matrix marker), indicated by the Pearson's correlation coefficient (r), was determined from maximum intensity projections of the Airyscan-processed images, using a "colocalization" function of the ZEN software. This approach allowed determination of the overlap between distinct mitochondrial subcompartments within the whole mitochondria. Therefore, the r values do not represent a colocalization between cytochrome c and ClpP but indicate spatial relation between the IMM and mitochondrial matrix in different samples. For quantifications of fluorescence profiles, single z-section Airyscan-processed images were used. The profiles along mitochondria were generated from the 2-channel images using the "profile" option available in the ZEN software. The data were tabularized and transferred to Microsoft Excel software (Microsoft), and the distance between highest fluorescence values was determined. For quantifications of TMRM fluorescence in time-lapse experiments, images were divided into four equally sized regions of interest, and fluorescence intensity of TMRM within each region of interest was determined using ZEN software. This approach, instead of measurements of single cells, helped reducing effects of cell movements. The data were tabularized and transferred to Microsoft Excel software (Microsoft) for further processing. Image cropping and global adjustments to brightness and contrast were performed using Adobe Photoshop CS6 software (Adobe Systems).

Proteomics

Whole mitochondria and LM fractions of WT and ATG5^{-/-} HCT116 cells treated with Acn or vehicle (DMSO) control were solubilized in 5% sodium deoxycholate after washing in PBS. Proteins were washed, reduced, alkylated, and trypsinolyzed on a filter as previously described (Huang et al., 2020). Tryptic peptides were separated on a nano-ACQUITY ultra performance liquid chromatography analytical column (Waters; BEH130 C18, 1.7 μm , 75 μm \times 200 mm) over a 165-min linear acetonitrile gradient (3–40%) with 0.1% formic acid on a Waters nano-ACQUITY ultra performance liquid chromatography system and analyzed on a coupled Thermo Fisher Scientific Orbitrap Fusion Lumos Tribrid mass spectrometer (Huang et al., 2020). MS1 scans were acquired at a resolution of 240,000, and

precursors were selected for fragmentation by higher-energy collisional dissociation (normalized collision energy at 32%) for a maximum 5-s cycle. Tandem mass spectra were searched against a UniProt *Homo sapiens* reference proteome with a maximum precursor mass error tolerance of 10 ppm and a maximum product mass error tolerance of 0.5 D in iontrap or 20 ppm in orbitrap, respectively. Cysteine alkylation by N-ethylmaleimide and iodoacetamide, deamidation of asparagine and glutamine, methionine oxidation, and diglycine-modified lysine were treated as dynamic modifications. Resulting hits were validated at a maximum false discovery rate of 0.01. Label-free quantifications were performed using Minora, an aligned accurate mass and retention time cluster quantification algorithm (Thermo Fisher Scientific). Samples were normalized by total protein. Peptide abundances were measured by the MS1 peak volumes of peptide ions, whose identities were confirmed by MS2 sequencing as described above. The localization probabilities of ubiquitination sites marked by diglycine were computed using a ptmRS algorithm (Taus et al., 2011).

Statistical calculations

Unless otherwise indicated, data were analyzed using an unpaired, two-tail Student's test; for multiple-group comparisons, data were analyzed using a one-way ANOVA with Bonferroni correction ($\alpha = 0.05$) to access significance. Where appropriate, nonparametric statistical hypothesis testing was performed with a Wilcoxon signed-rank test; for nonparametric multiple-groups comparisons, data were analyzed using a Kruskal-Wallis test with Dunn analysis ($\alpha = 0.05$) to access significance. The statistical analyses were performed using the MATLAB R2016a statistical package. All error bars are expressed as SD. P values > 0.05 were considered nonsignificant. N indicates independent experiments; n indicates repeats within each experiment.

Online supplemental material

Fig. S1 shows mosaic cytochrome c mitochondria formation in M17 neuroblastoma, HeLa, and Bax/Bak DKO HCT116 cells. OMM severing and IMM ubiquitination in Bax/Bak DKO HCT116 cells are also presented. Fig. S2 shows the roles of mitochondrial receptors of Drp1 on the mosaic distribution of cytochrome c in Acn-treated cells. Fig. S3 shows cytochrome c and Bax distribution in Acn- or ABT-737-treated WT and Bax/Bak DKO HCT116 cells. Caspase 9 activation and PARP1 cleavage in Acn- or ABT737 WT HCT116 cells are also shown. Fig. S4 shows that the expression of a dominant-negative mutant Drp1^{K38A} inhibits mosaic cytochrome c distribution and IMM ubiquitination in WT HCT116 cells. The inhibitory effect of CP on mosaic cytochrome c distribution in Acn-treated WT HCT116 cells is also shown. Fig. S5 shows a typical time-lapse experiment of WT HeLa cells transfected with cyt. c-GFP and labeled with TMRM. Fig. S6 shows that OMM severing and IMM ubiquitination occur in Acn-treated HeLa cells. Mosaic distribution of TRAP1 in HCT116 cells and CPOX in HeLa cells treated with Acn is also demonstrated. Expression levels of Parkin and CPOX in an array of cell lines are also presented. Video 1 shows mitochondrial changes in WT HeLa cells expressing mito-RED and cyt. c-GFP treated with Acn. Video 2 shows mitochondrial changes in Drp1^{-/-} HeLa cells

expressing mito-RED and cyt. c-GFP treated with Acn. **Video 3** shows mitochondrial changes in *Mff*^{-/-} HeLa expressing mito-RED and cyt. c-GFP treated with Acn. **Video 4** shows mitochondrial changes in *Drp1*^{-/-} HeLa cells expressing *Drp1*-mCherry and cyt. c-GFP treated with Acn. **Video 5** shows WT HeLa cells expressing mito-RED and cyt. c-GFP treated with FCCP. **Video 6** shows mitochondria changes in TMRM labeled WT HeLa cells expressing cyt. c-GFP cotreated with Acn and CP. **Video 7** shows mitochondrial alterations in TMRM labeled WT HeLa cells expressing cyt. c-GFP treated with Acn. **Video 8** shows mitochondrial alterations and subcellular localization of Parkin in WT HeLa cells expressing Parkin-mCherry and cyt. c-GFP treated with Acn. Data S1 contains original datasets from proteomic analyses of ubiquitinated proteins in membrane fractions from control or Acn-treated HCT116 cells.

Acknowledgments

We thank Agnieszka Lewandowska and Dr. Janet Shaw for sending us the *Drp1* receptor knockout MEFs; Dr. Mike Ryan, whose laboratory developed these cells; Dr. Richard J. Youle for ATG5^{-/-} HCT116, M17 neuroblastoma cells and fluorescent proteins-tagged Parkin vectors; and Dr. Nagendra Yadava for HA-tagged NDUF protein mammalian expression vectors.

Research reported in this paper was supported by the National Institutes of Health under awards R01GM129584 (M. Karbowski), R21NS096538 (B.M. Polster), and 1R01HL142290 (W.J. Lederer). This work was supported in part by the Center for Biomedical Engineering and Technology and the University of Maryland School of Pharmacy Mass Spectrometry Center (SOP1841-IQB2014).

The authors declare no competing financial interests.

Author contributions: Y. Oshima, E. Cartier, L. Boyman, N. Verhoeven, B.M. Polster, and M. Karbowski conducted the experiments and/or analyzed data. W. Huang and M. Kane performed and analyzed mass spectrometry data. W.J. Lederer was instrumental in imaging experiments. M. Karbowski designed the study, supervised the project, and wrote the manuscript. All authors commented on and critically influenced the manuscript.

Submitted: 9 June 2020

Revised: 2 February 2021

Accepted: 15 March 2021

References

Abeliovich, H., M. Zarei, K.T. Rigbolt, R.J. Youle, and J. Dengjel. 2013. Involvement of mitochondrial dynamics in the segregation of mitochondrial matrix proteins during stationary phase mitophagy. *Nat. Commun.* 4:2789. <https://doi.org/10.1038/ncomms3789>

Ashrafi, G., J.S. Schlehe, M.J. LaVoie, and T.L. Schwarz. 2014. Mitophagy of damaged mitochondria occurs locally in distal neuronal axons and requires PINK1 and Parkin. *J. Cell Biol.* 206:655–670. <https://doi.org/10.1083/jcb.201401070>

Ausenda, S., E. Di Pierro, V. Brancaleoni, D. Tavazzi, and M.D. Cappellini. 2009. Novel human pathological mutations. Gene symbol: CPOX. Disease: Coproporphyrin. *Hum. Genet.* 126:342.

Battersby, B.J., and U. Richter. 2013. Why translation counts for mitochondria - retrograde signalling links mitochondrial protein synthesis to mitochondrial biogenesis and cell proliferation. *J. Cell Sci.* 126:4331–4338. <https://doi.org/10.1242/jcs.131888>

Bingol, B., J.S. Tea, L. Phu, M. Reichelt, C.E. Bakalarski, Q. Song, O. Foreman, D.S. Kirkpatrick, and M. Sheng. 2014. The mitochondrial deubiquitinase USP30 opposes parkin-mediated mitophagy. *Nature.* 510:370–375. <https://doi.org/10.1038/nature13418>

Bonomini, F., L.F. Rodella, and R. Rezzani. 2015. Metabolic syndrome, aging and involvement of oxidative stress. *Aging Dis.* 6:109–120. <https://doi.org/10.14336/AD.2014.0305>

Boyman, L., M. Karbowski, and W.J. Lederer. 2020. Regulation of Mitochondrial ATP Production: Ca²⁺ Signaling and Quality Control. *Trends Mol. Med.* 26:21–39. <https://doi.org/10.1016/j.molmed.2019.10.007>

Breitenbach, M., M. Rinnerthaler, J. Hartl, A. Stincone, J. Vowinckel, H. Breitenbach-Koller, and M. Ralser. 2014. Mitochondria in ageing: there is metabolism beyond the ROS. *FEMS Yeast Res.* 14:198–212. <https://doi.org/10.1111/1567-1364.12134>

Burman, J.L., S. Pickles, C. Wang, S. Sekine, J.N.S. Vargas, Z. Zhang, A.M. Youle, C.L. Nezhich, X. Wu, J.A. Hammer, and R.J. Youle. 2017. Mitochondrial fission facilitates the selective mitophagy of protein aggregates. *J. Cell Biol.* 216:3231–3247. <https://doi.org/10.1083/jcb.201612106>

Caballero, A., A. Ugidos, B. Liu, D. Öling, K. Kvint, X. Hao, C. Mignat, L. Nachin, M. Molin, and T. Nyström. 2011. Absence of mitochondrial translation control proteins extends life span by activating sirT-independent silencing. *Mol. Cell.* 42:390–400. <https://doi.org/10.1016/j.molcel.2011.03.021>

Cai, Q., H.M. Zakaria, A. Simone, and Z.H. Sheng. 2012. Spatial parkin translocation and degradation of damaged mitochondria via mitophagy in live cortical neurons. *Curr. Biol.* 22:545–552. <https://doi.org/10.1016/j.cub.2012.02.005>

Canet-Avilés, R.M., M.A. Wilson, D.W. Miller, R. Ahmad, C. McLendon, S. Bandyopadhyay, M.J. Baptista, D. Ringe, G.A. Petsko, and M.R. Cookson. 2004. The Parkinson's disease protein DJ-1 is neuroprotective due to cysteine-sulfenic acid-driven mitochondrial localization. *Proc. Natl. Acad. Sci. USA.* 101:9103–9108. <https://doi.org/10.1073/pnas.0402959101>

Chan, N.C., A.M. Salazar, A.H. Pham, M.J. Sweredoski, N.J. Kolawa, R.L. Graham, S. Hess, and D.C. Chan. 2011. Broad activation of the ubiquitin-proteasome system by Parkin is critical for mitophagy. *Hum. Mol. Genet.* 20:1726–1737. <https://doi.org/10.1093/hmg/ddr048>

Cherok, E., S. Xu, S. Li, S. Das, W.A. Meltzer, M. Zalzman, C. Wang, and M. Karbowski. 2017. Novel regulatory roles of Mff and Drp1 in E3 ubiquitin ligase MARCH5-dependent degradation of MiD49 and Mcl1 and control of mitochondrial dynamics. *Mol. Biol. Cell.* 28:396–410. <https://doi.org/10.1091/mbc.e16-04-0208>

Cho, H.M., J.R. Ryu, Y. Jo, T.W. Seo, Y.N. Choi, J.H. Kim, J.M. Chung, B. Cho, H.C. Kang, S.W. Yu, et al. 2019. Drp1-Zip1 Interaction Regulates Mitochondrial Quality Surveillance System. *Mol. Cell.* 73:364–376.e8. <https://doi.org/10.1016/j.molcel.2018.11.009>

Cogliati, S., J.A. Enriquez, and L. Scorrano. 2016. Mitochondrial Cristae: Where Beauty Meets Functionality. *Trends Biochem. Sci.* 41:261–273. <https://doi.org/10.1016/j.tibs.2016.01.001>

Collins, T.J., M.J. Berridge, P. Lipp, and M.D. Bootman. 2002. Mitochondria are morphologically and functionally heterogeneous within cells. *EMBO J.* 21:1616–1627. <https://doi.org/10.1093/emboj/21.7.1616>

Currais, A. 2015. Ageing and inflammation - A central role for mitochondria in brain health and disease. *Ageing Res. Rev.* 21:30–42. <https://doi.org/10.1016/j.arr.2015.02.001>

Fang, E.F., Y. Hou, K. Palikaras, B.A. Adriaanse, J.S. Kerr, B. Yang, S. Lautrup, M.M. Hasan-Olive, D. Caponio, X. Dan, et al. 2019. Mitophagy inhibits amyloid- β and tau pathology and reverses cognitive deficits in models of Alzheimer's disease. *Nat. Neurosci.* 22:401–412. <https://doi.org/10.1038/s41593-018-0332-9>

Friedman, J.R., and J. Nunnari. 2014. Mitochondrial form and function. *Nature.* 505:335–343. <https://doi.org/10.1038/nature12985>

Friedman, J.R., L.L. Lackner, M. West, J.R. DiBenedetto, J. Nunnari, and G.K. Voeltz. 2011. ER tubules mark sites of mitochondrial division. *Science.* 334:358–362. <https://doi.org/10.1126/science.1207385>

Gammage, P.A., J. Rorbach, A.I. Vincent, E.J. Rebar, and M. Minczuk. 2014. Mitochondrially targeted ZFNs for selective degradation of pathogenic mitochondrial genomes bearing large-scale deletions or point mutations. *EMBO Mol. Med.* 6:458–466. <https://doi.org/10.1002/emmm.201303672>

Gandre-Babbe, S., and A.M. van der Blik. 2008. The novel tail-anchored membrane protein Mff controls mitochondrial and peroxisomal fission in mammalian cells. *Mol. Biol. Cell.* 19:2402–2412. <https://doi.org/10.1091/mbc.e07-12-1287>

Goldstein, J.C., N.J. Waterhouse, P. Juin, G.I. Evan, and D.R. Green. 2000. The coordinate release of cytochrome c during apoptosis is rapid, complete

- and kinetically invariant. *Nat. Cell Biol.* 2:156–162. <https://doi.org/10.1038/35004029>
- Grandchamp, B., N. Phung, and Y. Nordmann. 1978. The mitochondrial localization of coproporphyrinogen III oxidase. *Biochem. J.* 176:97–102. <https://doi.org/10.1042/bj1760097>
- Große, L., C.A. Wurm, C. Brüser, D. Neumann, D.C. Jans, and S. Jakobs. 2016. Bax assembles into large ring-like structures remodeling the mitochondrial outer membrane in apoptosis. *EMBO J.* 35:402–413. <https://doi.org/10.15252/embj.201592789>
- Heo, J.M., N. Livnat-Levanon, E.B. Taylor, K.T. Jones, N. Dephoure, J. Ring, J. Xie, J.L. Brodsky, F. Madeo, S.P. Gygi, et al. 2010. A stress-responsive system for mitochondrial protein degradation. *Mol. Cell.* 40:465–480. <https://doi.org/10.1016/j.molcel.2010.10.021>
- Huang, W., J. Yu, T. Liu, A.E. Defnet, S. Zalesak, A.M. Farese, T.J. MacVittie, and M.A. Kane. 2020. Proteomics of Non-human Primate Plasma after Partial-body Radiation with Minimal Bone Marrow Sparing. *Health Phys.* 119:621–632. <https://doi.org/10.1097/HP.0000000000001350>
- Hughes, A.L., C.E. Hughes, K.A. Henderson, N. Yazvenko, and D.E. Gottschling. 2016. Selective sorting and destruction of mitochondrial membrane proteins in aged yeast. *eLife.* 5:e13943. <https://doi.org/10.7554/eLife.13943>
- Kageyama, Y., M. Hoshijima, K. Seo, D. Bedja, P. Sysa-Shah, S.A. Andrabi, W. Chen, A. Höke, V.L. Dawson, T.M. Dawson, et al. 2014. Parkin-independent mitophagy requires Drp1 and maintains the integrity of mammalian heart and brain. *EMBO J.* 33:2798–2813. <https://doi.org/10.15252/embj.201488658>
- Kane, L.A., M. Lazarou, A.I. Fogel, Y. Li, K. Yamano, S.A. Sarraf, S. Banerjee, and R.J. Youle. 2014. PINK1 phosphorylates ubiquitin to activate Parkin E3 ubiquitin ligase activity. *J. Cell Biol.* 205:143–153. <https://doi.org/10.1083/jcb.201402104>
- Karbowski, M., and R.J. Youle. 2011. Regulating mitochondrial outer membrane proteins by ubiquitination and proteasomal degradation. *Curr. Opin. Cell Biol.* 23:476–482. <https://doi.org/10.1016/j.cob.2011.05.007>
- Karbowski, M., Y.J. Lee, B. Gaume, S.Y. Jeong, S. Frank, A. Nechushtan, A. Santel, M. Fuller, C.L. Smith, and R.J. Youle. 2002. Spatial and temporal association of Bax with mitochondrial fission sites, Drp1, and Mfn2 during apoptosis. *J. Cell Biol.* 159:931–938. <https://doi.org/10.1083/jcb.200209124>
- Karbowski, M., A. Neutzner, and R.J. Youle. 2007. The mitochondrial E3 ubiquitin ligase MARCH5 is required for Drp1 dependent mitochondrial division. *J. Cell Biol.* 178:71–84. <https://doi.org/10.1083/jcb.200611064>
- Kim, G.H., J.E. Kim, S.J. Rhie, and S. Yoon. 2015. The Role of Oxidative Stress in Neurodegenerative Diseases. *Exp. Neurobiol.* 24:325–340. <https://doi.org/10.5607/en.2015.24.4.325>
- Koyano, F., K. Okatsu, H. Kosako, Y. Tamura, E. Go, M. Kimura, Y. Kimura, H. Tsuchiya, H. Yoshihara, T. Hirokawa, et al. 2014. Ubiquitin is phosphorylated by PINK1 to activate parkin. *Nature.* 510:162–166. <https://doi.org/10.1038/nature13392>
- Kuznetsov, A.V., and R. Margreiter. 2009. Heterogeneity of mitochondria and mitochondrial function within cells as another level of mitochondrial complexity. *Int. J. Mol. Sci.* 10:1911–1929. <https://doi.org/10.3390/ijms10041911>
- Lazarou, M., D.A. Sliter, L.A. Kane, S.A. Sarraf, C. Wang, J.L. Burman, D.P. Sideris, A.I. Fogel, and R.J. Youle. 2015. The ubiquitin kinase PINK1 recruits autophagy receptors to induce mitophagy. *Nature.* 524:309–314. <https://doi.org/10.1038/nature14893>
- Lee, J.J., A. Sanchez-Martinez, A. Martinez Zarate, C. Benincá, U. Mayor, M.J. Clague, and A.J. Whitworth. 2018. Basal mitophagy is widespread in *Drosophila* but minimally affected by loss of Pink1 or parkin. *J. Cell Biol.* 217:1613–1622. <https://doi.org/10.1083/jcb.201801044>
- Liang, J.R., A. Martinez, J.D. Lane, U. Mayor, M.J. Clague, and S. Urbé. 2015. USP30 deubiquitylates mitochondrial Parkin substrates and restricts apoptotic cell death. *EMBO Rep.* 16:618–627. <https://doi.org/10.15252/embr.201439820>
- Manzanillo, P.S., J.S. Ayres, R.O. Watson, A.C. Collins, G. Souza, C.S. Rae, D.S. Schneider, K. Nakamura, M.U. Shiloh, and J.S. Cox. 2013. The ubiquitin ligase parkin mediates resistance to intracellular pathogens. *Nature.* 501:512–516. <https://doi.org/10.1038/nature12566>
- McArthur, K., L.W. Whitehead, J.M. Heddleston, L. Li, B.S. Padman, V. Oorschot, N.D. Geoghegan, S. Chappaz, S. Davidson, H. San Chin, et al. 2018. BAK/BAX macropores facilitate mitochondrial herniation and mtDNA efflux during apoptosis. *Science.* 359:eaao6047. <https://doi.org/10.1126/science.aao6047>
- McLelland, G.L., T. Goiran, W. Yi, G. Dorval, C.X. Chen, N.D. Lauinger, A.I. Krahn, S. Valimehr, A. Rakovic, I. Rouiller, et al. 2018. Mfn2 ubiquitination by PINK1/parkin gates the p97-dependent release of ER from mitochondria to drive mitophagy. *eLife.* 7:e32866. <https://doi.org/10.7554/eLife.32866>
- McWilliams, T.G., A.R. Prescott, L. Montava-Garriga, G. Ball, F. Singh, E. Barini, M.M.K. Muqit, S.P. Brooks, and I.G. Ganley. 2018. Basal Mitophagy Occurs Independently of PINK1 in Mouse Tissues of High Metabolic Demand. *Cell Metab.* 27:439–449.e5. <https://doi.org/10.1016/j.cmet.2017.12.008>
- Medlock, A.E., M.T. Shiferaw, J.R. Marcero, A.A. Vashisht, J.A. Wohlschlegel, J.D. Phillips, and H.A. Dailey. 2015. Identification of the Mitochondrial Heme Metabolism Complex. *PLoS One.* 10:e0135896. <https://doi.org/10.1371/journal.pone.0135896>
- Moretton, A., F. Morel, B. Macao, P. Lachaume, L. Ishak, M. Lefebvre, I. Garreau-Balandier, P. Vernet, M. Falkenberg, and G. Farge. 2017. Selective mitochondrial DNA degradation following double-strand breaks. *PLoS One.* 12:e0176795. <https://doi.org/10.1371/journal.pone.0176795>
- Nakamura, N., and S. Hirose. 2008. Regulation of mitochondrial morphology by USP30, a deubiquitinating enzyme present in the mitochondrial outer membrane. *Mol. Biol. Cell.* 19:1903–1911. <https://doi.org/10.1091/mbc.e07-11-1103>
- Narendra, D., A. Tanaka, D.F. Suen, and R.J. Youle. 2008. Parkin is recruited selectively to impaired mitochondria and promotes their autophagy. *J. Cell Biol.* 183:795–803. <https://doi.org/10.1083/jcb.200809125>
- Nechushtan, A., C.L. Smith, Y.T. Hsu, and R.J. Youle. 1999. Conformation of the Bax C-terminus regulates subcellular location and cell death. *EMBO J.* 18:2330–2341. <https://doi.org/10.1093/emboj/18.9.2330>
- Okatsu, K., F. Koyano, M. Kimura, H. Kosako, Y. Saeki, K. Tanaka, and N. Matsuda. 2015. Phosphorylated ubiquitin chain is the genuine Parkin receptor. *J. Cell Biol.* 209:111–128. <https://doi.org/10.1083/jcb.201410050>
- Osellame, L.D., A.P. Singh, D.A. Stroud, C.S. Palmer, D. Stojanovski, R. Ramachandran, and M.T. Ryan. 2016. Cooperative and independent roles of the Drp1 adaptors Mff, MiD49 and MiD51 in mitochondrial fission. *J. Cell Sci.* 129:2170–2181. <https://doi.org/10.1242/jcs.185165>
- Ott, M., B. Zhivotovsky, and S. Orrenius. 2007. Role of cardiolipin in cytochrome c release from mitochondria. *Cell Death Differ.* 14:1243–1247. <https://doi.org/10.1038/sj.cdd.4402135>
- Palmer, C.S., K.D. Elgass, R.G. Parton, L.D. Osellame, D. Stojanovski, and M.T. Ryan. 2013. Adaptor proteins MiD49 and MiD51 can act independently of Mff and Fis1 in Drp1 recruitment and are specific for mitochondrial fission. *J. Biol. Chem.* 288:27584–27593. <https://doi.org/10.1074/jbc.M113.479873>
- Paradies, G., V. Paradies, F.M. Ruggiero, and G. Petrosillo. 2014. Cardiolipin and mitochondrial function in health and disease. *Antioxid. Redox Signal.* 20:1925–1953. <https://doi.org/10.1089/ars.2013.5280>
- Perez, F.A., and R.D. Palmiter. 2005. Parkin-deficient mice are not a robust model of parkinsonism. *Proc. Natl. Acad. Sci. USA.* 102:2174–2179. <https://doi.org/10.1073/pnas.0409598102>
- Piekutowska-Abramczuk, D., Z. Assouline, L. Mataković, R.G. Feichtinger, E. Koňariková, E. Jurkiewicz, P. Stawiński, M. Gusic, A. Koller, A. Pollak, et al. 2018. NDUFB8 Mutations Cause Mitochondrial Complex I Deficiency in Individuals with Leigh-like Encephalomyopathy. *Am. J. Hum. Genet.* 102:460–467. <https://doi.org/10.1016/j.ajhg.2018.01.008>
- Pridgeon, J.W., J.A. Olzmann, L.S. Chin, and L. Li. 2007. PINK1 protects against oxidative stress by phosphorylating mitochondrial chaperone TRAP1. *PLoS Biol.* 5:e172. <https://doi.org/10.1371/journal.pbio.0050172>
- Radoshevich, L., L. Murrow, N. Chen, E. Fernandez, S. Roy, C. Fung, and J. Debnath. 2010. ATG12 conjugation to ATG3 regulates mitochondrial homeostasis and cell death. *Cell.* 142:590–600. <https://doi.org/10.1016/j.cell.2010.07.018>
- Richter, U., T. Lahtinen, P. Marttinen, M. Myöhänen, D. Greco, G. Cannino, H.T. Jacobs, N. Lietzén, T.A. Nyman, and B.J. Battersby. 2013. A mitochondrial ribosomal and RNA decay pathway blocks cell proliferation. *Curr. Biol.* 23:535–541. <https://doi.org/10.1016/j.cub.2013.02.019>
- Richter, U., T. Lahtinen, P. Marttinen, F. Suomi, and B.J. Battersby. 2015. Quality control of mitochondrial protein synthesis is required for membrane integrity and cell fitness. *J. Cell Biol.* 211:373–389. <https://doi.org/10.1083/jcb.201504062>
- Sarraf, S.A., M. Raman, V. Guarani-Pereira, M.E. Sowa, E.L. Huttlin, S.P. Gygi, and J.W. Harper. 2013. Landscape of the PARKIN-dependent ubiquitylome in response to mitochondrial depolarization. *Nature.* 496:372–376. <https://doi.org/10.1038/nature12043>
- Scheibye-Knudsen, M., E.F. Fang, D.L. Croteau, D.M. Wilson III, and V.A. Bohr. 2015. Protecting the mitochondrial powerhouse. *Trends Cell Biol.* 25:158–170. <https://doi.org/10.1016/j.tcb.2014.11.002>
- Scorrano, L., M. Ashiya, K. Buttle, S. Weiler, S.A. Oakes, C.A. Mannella, and S.J. Korsmeyer. 2002. A distinct pathway remodels mitochondrial

- cristae and mobilizes cytochrome c during apoptosis. *Dev. Cell.* 2:55–67. [https://doi.org/10.1016/S1534-5807\(01\)00116-2](https://doi.org/10.1016/S1534-5807(01)00116-2)
- Sheth, A., S. Escobar-Alvarez, J. Gardner, L. Ran, M.L. Heaney, and D.A. Scheinberg. 2014. Inhibition of human mitochondrial peptide deformylase causes apoptosis in c-myc-overexpressing hematopoietic cancers. *Cell Death Dis.* 5:e1152. <https://doi.org/10.1038/cddis.2014.112>
- Skrčić, M., S. Sriskanthadevan, B. Jhas, M. Gebbia, X. Wang, Z. Wang, R. Hurren, Y. Jitkova, M. Gronda, N. Maclean, et al. 2011. Inhibition of mitochondrial translation as a therapeutic strategy for human acute myeloid leukemia. *Cancer Cell.* 20:674–688. <https://doi.org/10.1016/j.ccr.2011.10.015>
- Smirnova, E., L. Griparic, D.L. Shurland, and A.M. van der Bliek. 2001. Dynamin-related protein Drp1 is required for mitochondrial division in mammalian cells. *Mol. Biol. Cell.* 12:2245–2256. <https://doi.org/10.1091/mbc.12.8.2245>
- Smits, P., J. Smeitink, and L. van den Heuvel. 2010. Mitochondrial translation and beyond: processes implicated in combined oxidative phosphorylation deficiencies. *J. Biomed. Biotechnol.* 2010:737385. <https://doi.org/10.1155/2010/737385>
- Spadafora, D., N. Kozhukhar, V.N. Chouljenko, K.G. Kousoulas, and M.F. Alexeyev. 2016. Methods for Efficient Elimination of Mitochondrial DNA from Cultured Cells. *PLoS One.* 11:e0154684. <https://doi.org/10.1371/journal.pone.0154684>
- Suhm, T., J.M. Kaimal, H. Dawitz, C. Peselj, A.E. Masser, S. Hanzén, M. Ambrožič, A. Smialowska, M.L. Björck, P. Brzezinski, et al. 2018. Mitochondrial Translation Efficiency Controls Cytoplasmic Protein Homeostasis. *Cell Metab.* 27:1309–1322.e6. <https://doi.org/10.1016/j.cmet.2018.04.011>
- Tanaka, A., M.M. Cleland, S. Xu, D.P. Narendra, D.F. Suen, M. Karbowski, and R.J. Youle. 2010. Proteasome and p97 mediate mitophagy and degradation of mitofusins induced by Parkin. *J. Cell Biol.* 191:1367–1380. <https://doi.org/10.1083/jcb.201007013>
- Taus, T., T. Köcher, P. Pichler, C. Paschke, A. Schmidt, C. Henrich, and K. Mechtler. 2011. Universal and confident phosphorylation site localization using phosphoRS. *J. Proteome Res.* 10:5354–5362. <https://doi.org/10.1021/pr200611n>
- Twig, G., A. Elorza, A.J. Molina, H. Mohamed, J.D. Wikstrom, G. Walzer, L. Stiles, S.E. Haigh, S. Katz, G. Las, et al. 2008. Fission and selective fusion govern mitochondrial segregation and elimination by autophagy. *EMBO J.* 27:433–446. <https://doi.org/10.1038/sj.emboj.7601963>
- Villa, E., E. Proïcs, C. Rubio-Patiño, S. Obba, B. Zunino, J.P. Bossowski, R.M. Rozier, J. Chiche, L. Mondragón, J.S. Riley, et al. 2017. Parkin-Independent Mitophagy Controls Chemotherapeutic Response in Cancer Cells. *Cell Rep.* 20:2846–2859. <https://doi.org/10.1016/j.celrep.2017.08.087>
- Vogel, F., C. Bornhövd, W. Neupert, and A.S. Reichert. 2006. Dynamic sub-compartmentalization of the mitochondrial inner membrane. *J. Cell Biol.* 175:237–247. <https://doi.org/10.1083/jcb.200605138>
- Wang, C., and R.J. Youle. 2012. Predominant requirement of Bax for apoptosis in HCT116 cells is determined by Mcl-1's inhibitory effect on Bak. *Oncogene.* 31:3177–3189. <https://doi.org/10.1038/onc.2011.497>
- Xu, S., G. Peng, Y. Wang, S. Fang, and M. Karbowski. 2011. The AAA-ATPase p97 is essential for outer mitochondrial membrane protein turnover. *Mol. Biol. Cell.* 22:291–300. <https://doi.org/10.1091/mbc.e10-09-0748>
- Xu, S., E. Cherok, S. Das, S. Li, B.A. Roelofs, S.X. Ge, B.M. Polster, L. Boyman, W.J. Lederer, C. Wang, and M. Karbowski. 2016. Mitochondrial E3 ubiquitin ligase MARCH5 controls mitochondrial fission and cell sensitivity to stress-induced apoptosis through regulation of Mif49 protein. *Mol. Biol. Cell.* 27:349–359. <https://doi.org/10.1091/mbc.e15-09-0678>
- Yamada, T., D. Murata, Y. Adachi, K. Itoh, S. Kameoka, A. Igarashi, T. Kato, Y. Araki, R.L. Haganir, T.M. Dawson, et al. 2018. Mitochondrial Stasis Reveals p62-Mediated Ubiquitination in Parkin-Independent Mitophagy and Mitigates Nonalcoholic Fatty Liver Disease. *Cell Metab.* 28:588–604.e5. <https://doi.org/10.1016/j.cmet.2018.06.014>
- Yonashiro, R., S. Ishido, S. Kyo, T. Fukuda, E. Goto, Y. Matsuki, M. Ohmura-Hoshino, K. Sada, H. Hotta, H. Yamamura, et al. 2006. A novel mitochondrial ubiquitin ligase plays a critical role in mitochondrial dynamics. *EMBO J.* 25:3618–3626. <https://doi.org/10.1038/sj.emboj.7601249>
- Yoshii, S.R., C. Kishi, N. Ishihara, and N. Mizushima. 2011. Parkin mediates proteasome-dependent protein degradation and rupture of the outer mitochondrial membrane. *J. Biol. Chem.* 286:19630–19640. <https://doi.org/10.1074/jbc.M110.209338>
- Zheng, Y.T., S. Shahnazari, A. Brech, T. Lamark, T. Johansen, and J.H. Brummell. 2009. The adaptor protein p62/SQSTM1 targets invading bacteria to the autophagy pathway. *J. Immunol.* 183:5909–5916. <https://doi.org/10.4049/jimmunol.0900441>
- Zick, M., R. Rabl, and A.S. Reichert. 2009. Cristae formation-linking ultra-structure and function of mitochondria. *Biochim. Biophys. Acta.* 1793:5–19. <https://doi.org/10.1016/j.bbamcr.2008.06.013>

Supplemental material

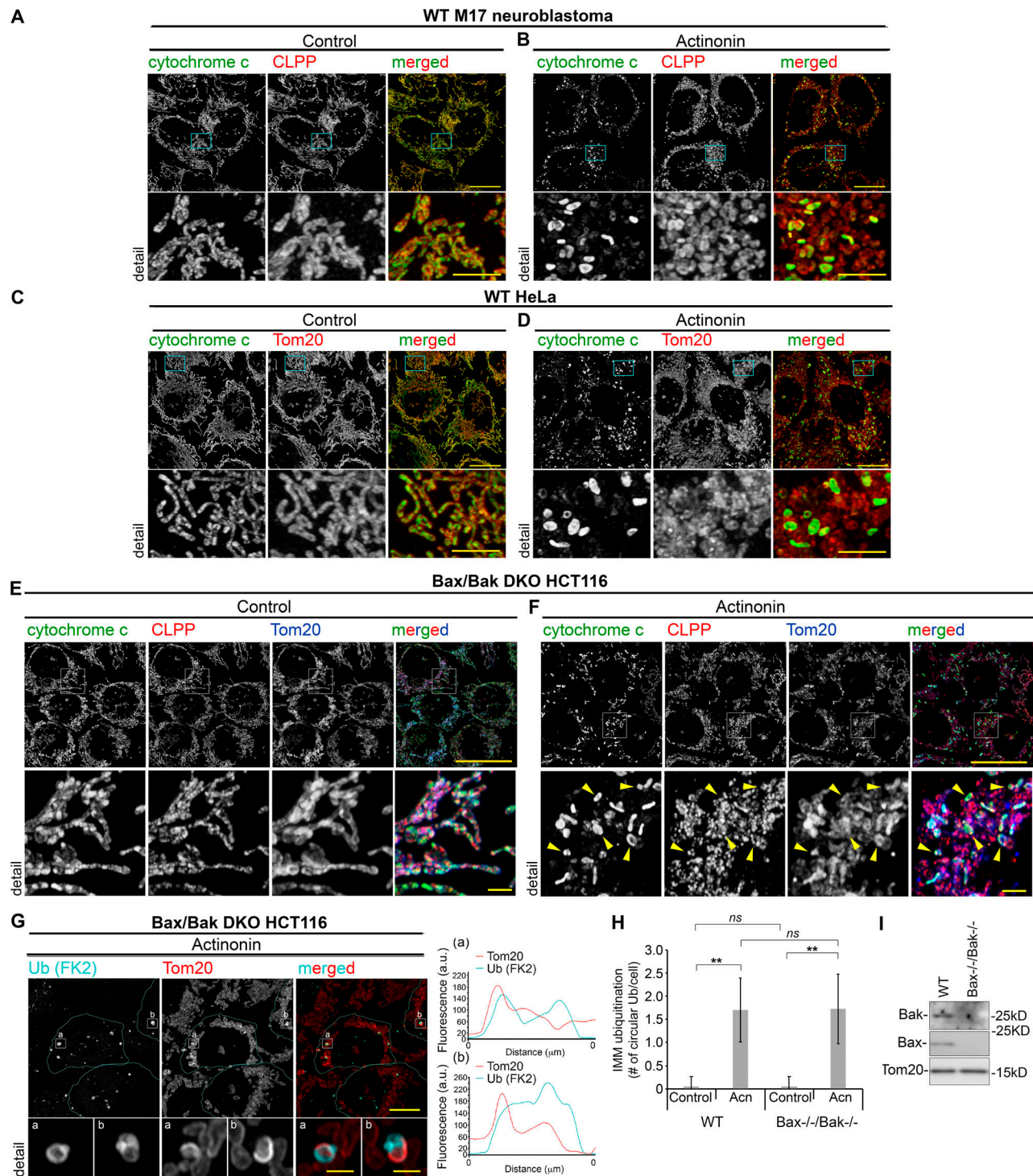


Figure S1. Induction of mosaic cytochrome c distribution in neuroblastoma, HeLa cells, and Bax/Bak DKO HCT116 cells. (A–D) M17 neuroblastoma (A and B) and HeLa (C and D) cells were treated with DMSO (control; A and C) or Acn (B and D) for 6 h, followed by immunostaining to detect cytochrome c (green in A–D), ClpP (red in A and B), and Tom20 (red in C and D) and Airyscan image acquisition. Detail images are from areas outlined with light blue rectangles. Scale bars represent 20 μm (5 μm in detail images). (E–I) Depletion of Bax and Bak does not affect Acn-induced mosaic distribution of cytochrome c, OMM severing and IMM ubiquitination. Bax^{-/-}/Bak^{-/-} DKO HCT116 cells were treated with DMSO (vehicle; E) or Acn (F) for 6 h, followed by immunostaining to detect cytochrome c (green), ClpP (red), and Tom20 (blue) and Airyscan image acquisition. Arrowheads in F (detail) point to the high-cytochrome c mitochondria. Scale bars represent 20 μm (2 μm in detail images). (G) Bax^{-/-}/Bak^{-/-} DKO cells treated with Acn for 6 h were immunostained to detect Ub (anti-Ub FK2 mAb; light blue) and Tom20 (red) followed by image acquisition. High magnification of areas marked with rectangles are shown in “detail” images a and b. Scale bars represent 10 μm (1 μm in detail images; a and b). (H) Quantification of circular Ub FK2-positive structures in control and Acn-treated WT and Bax^{-/-}/Bak^{-/-} DKO cells. Data represent mean \pm SD; $n = 50$ cells per condition. Similar results were obtained in $n = 3$ independent experiments. **, $P < 0.01$; ns indicates nonsignificant; one-way ANOVA with Bonferroni correction ($\alpha = 0.05$). (I) Western blot analysis of expression levels of Bax and Bak in WT and Bax^{-/-}/Bak^{-/-} DKO cells. Tom20 was used as a loading control.

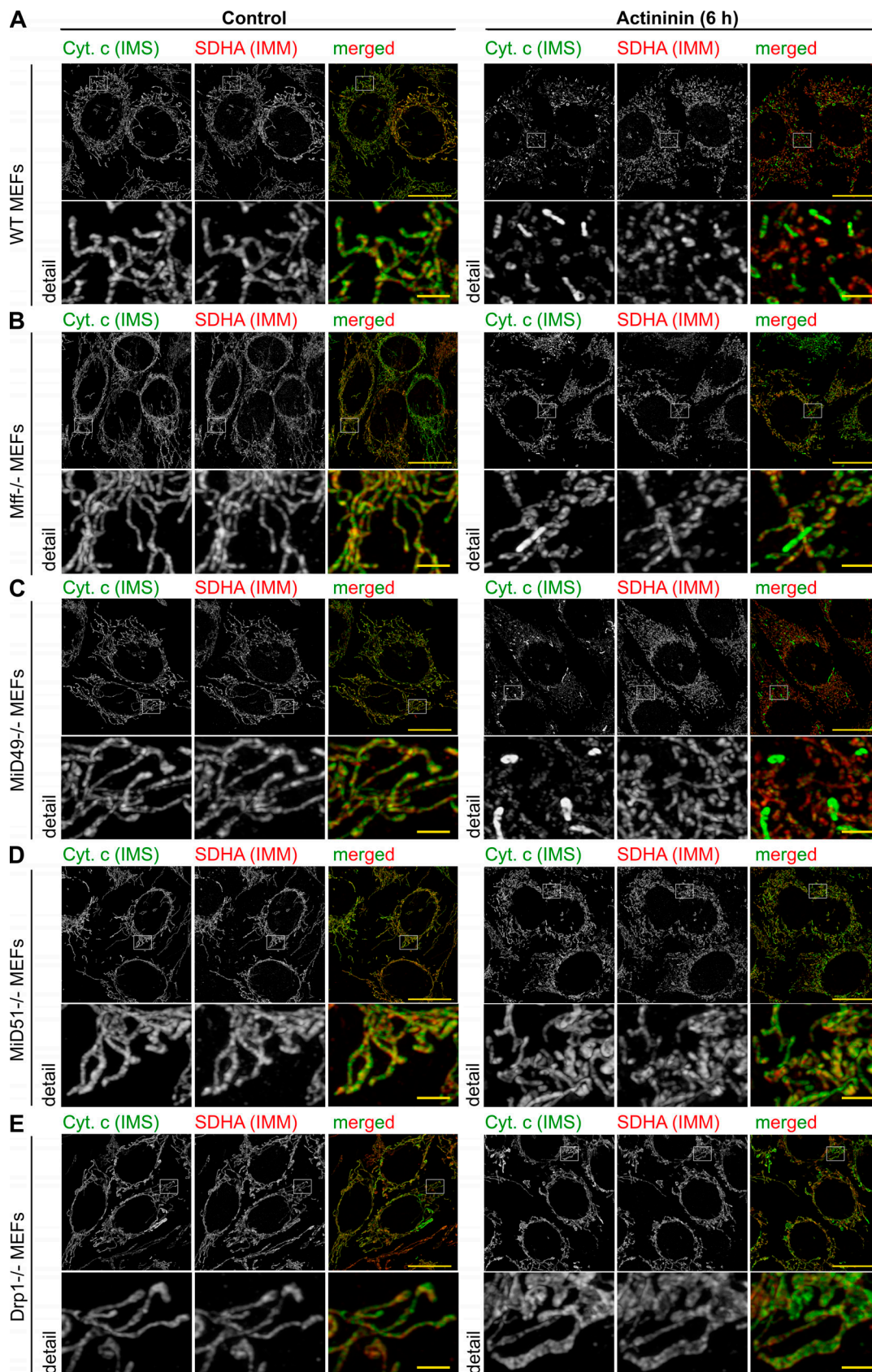


Figure S2. **Control of mosaic cytochrome c distribution by Drp1 and mitochondrial Drp1 receptors.** (A–E) WT (A), Mff^{-/-} (B), MiD49^{-/-} (C), MiD51^{-/-} (D), and Drp1^{-/-} (E) MEFs were treated with DMSO (control; left panels in A–E) or Acn (right panels in A–E) for 6 h. Typical examples of cells immunostained to detect cytochrome c (green) and Tom20 (red) are shown. Scale bars represent 20 μ m (2 μ m in detail images).

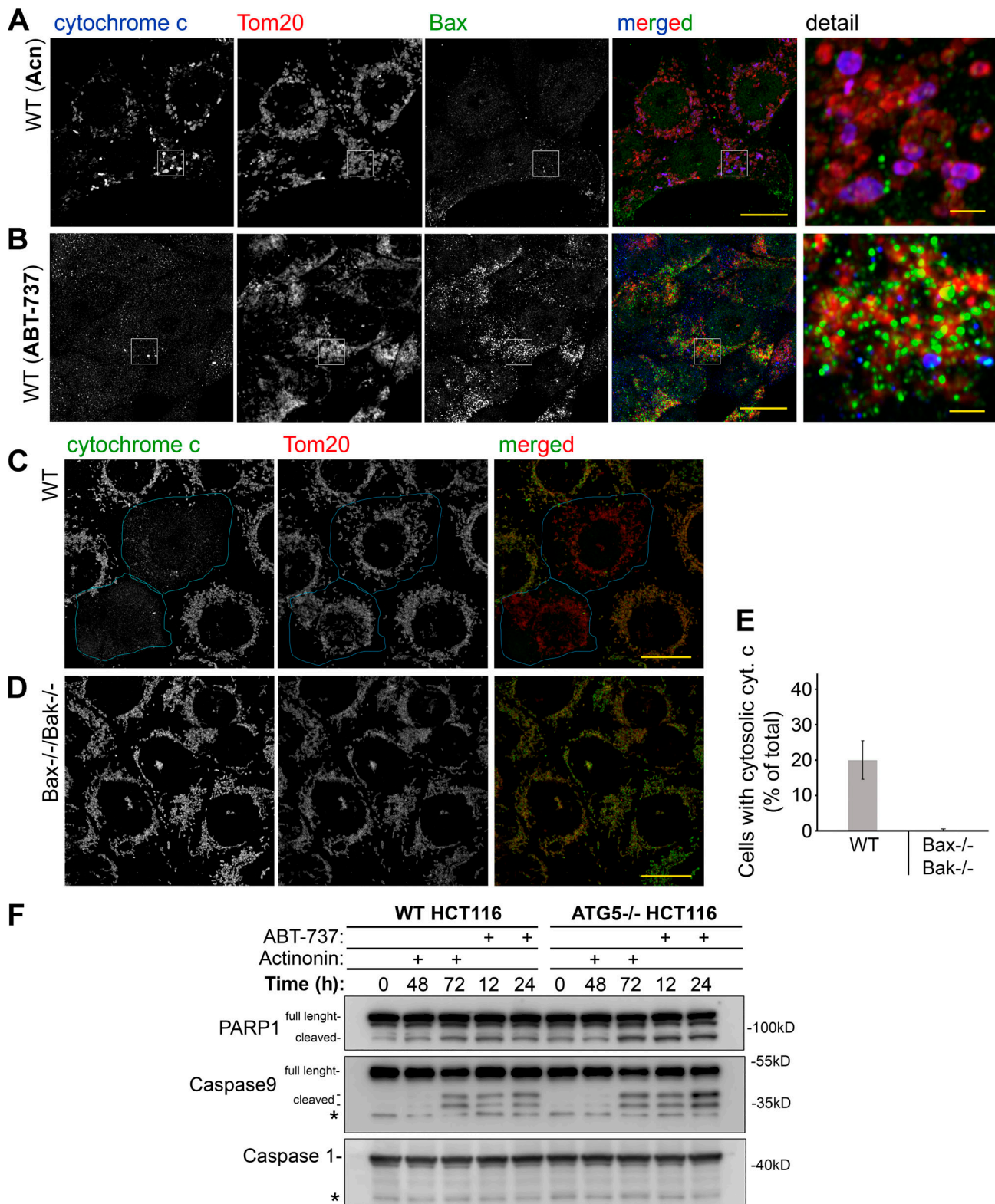


Figure S3. **Cytochrome c, Bax, and apoptosis in Acn- and ABT-737-treated cells. (A and B)** WT HCT116 cells treated with Acn (A) or ABT-737 (B) for 6 h were immunostained to detect cytochrome c (blue), Tom 20 (red) and Bax (green), followed by Airyscan imaging. Consistent data were obtained in $n = 3$ independent experiments. Scale bars represent 10 μm , and 1.0 μm in detail images. **(C and D)** Imaging of cytochrome c in apoptotic cells. To induce apoptotic OMM permeabilization WT (C) and Bax^{-/-}/Bak^{-/-} DKO (D) cells were treated with ABT-737 for 6 h. Cells were immunostained to detect cytochrome c (green) and Tom20 (red). Scale bars represent 10 μm . **(E)** Number of cells showing cytosolic cytochrome c (as in cells traced with blue lines in C) were quantified. Data represent mean \pm SD; $n = 150$. **(F)** Western blot analyses of caspase 9 and PARP in WT and ATG5^{-/-} HCT116 cells treated as indicated in the figure. Asterisks indicate nonspecific proteins detected by anti-caspase 9 and anti-caspase 1 antibodies. Caspase 1, which was not detectably processed, was used as a loading control.

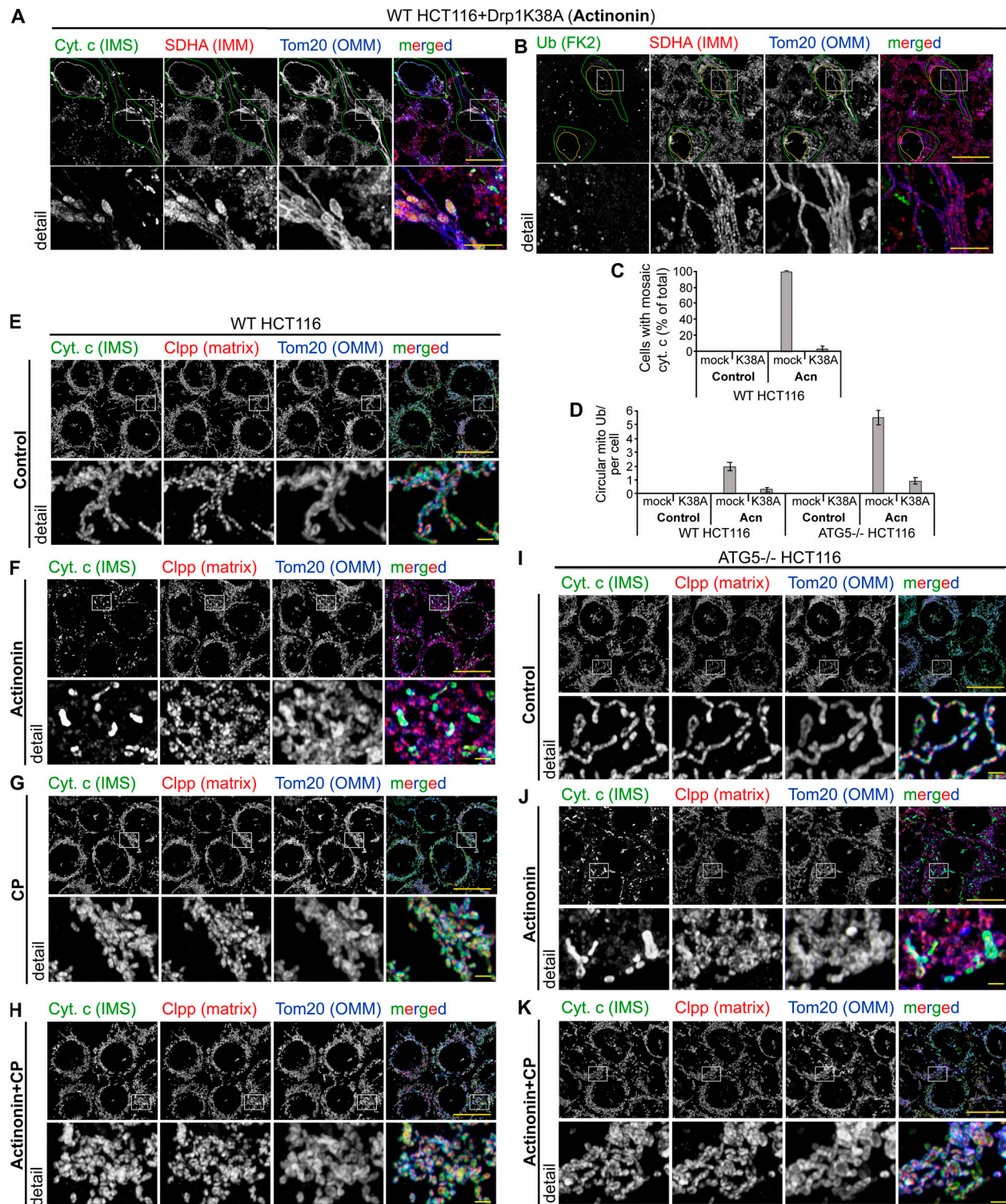


Figure S4. **Critical roles of mitochondrial fission and mitochondrial translation in mitochondrial alterations induced by reduced MTF. (A and B)** Typical images of dominant-negative mutant of Drp1 (Drp1^{K38A})-transfected WT HCT116 cells treated with Acn for 6 h and immunolabeled to detect cytochrome c (green in merged images in A), conjugated Ub (FK2; green in merged images in B), SDHA (red in merged images in A and B), and Tom20 (blue in merged images in A and B). Drp1^{K38A}-expressing cells are traced with green (A and B) and nuclei (B) with yellow lines. Detail images are from areas outlined with white rectangles. Scale bars represent 20 μ m (5 μ m in detail images). **(C)** Quantification of “high”-cytochrome c mitochondria in mock- and Drp1^{K38A}-transfected WT HCT116 treated with Acn for 6 h. Data represent mean \pm SD; $n = 3$ ($n = 100$ cells). **(D)** Quantification of circular mitochondrial ubiquitination in mock- and Drp1^{K38A}-transfected WT and ATG5^{-/-} cells treated with Acn for 6 h. Data represent mean \pm SD; $n = 4$; ($n = 100$ cells). **(E–K)** WT (E–H) and ATG5^{-/-} HCT116 cells (I–K) cells were treated with DMSO (control; E and I), Acn (F and J), CP (G), and Acn plus CP (H and K) for 6 h, followed by immunostaining to detect cytochrome c (IMS marker, green), ClpP (matrix marker; red), and Tom20 (OMM marker; blue) and Airyscan image acquisition. Scale bars represent 20 μ m (2 μ m in detail images).

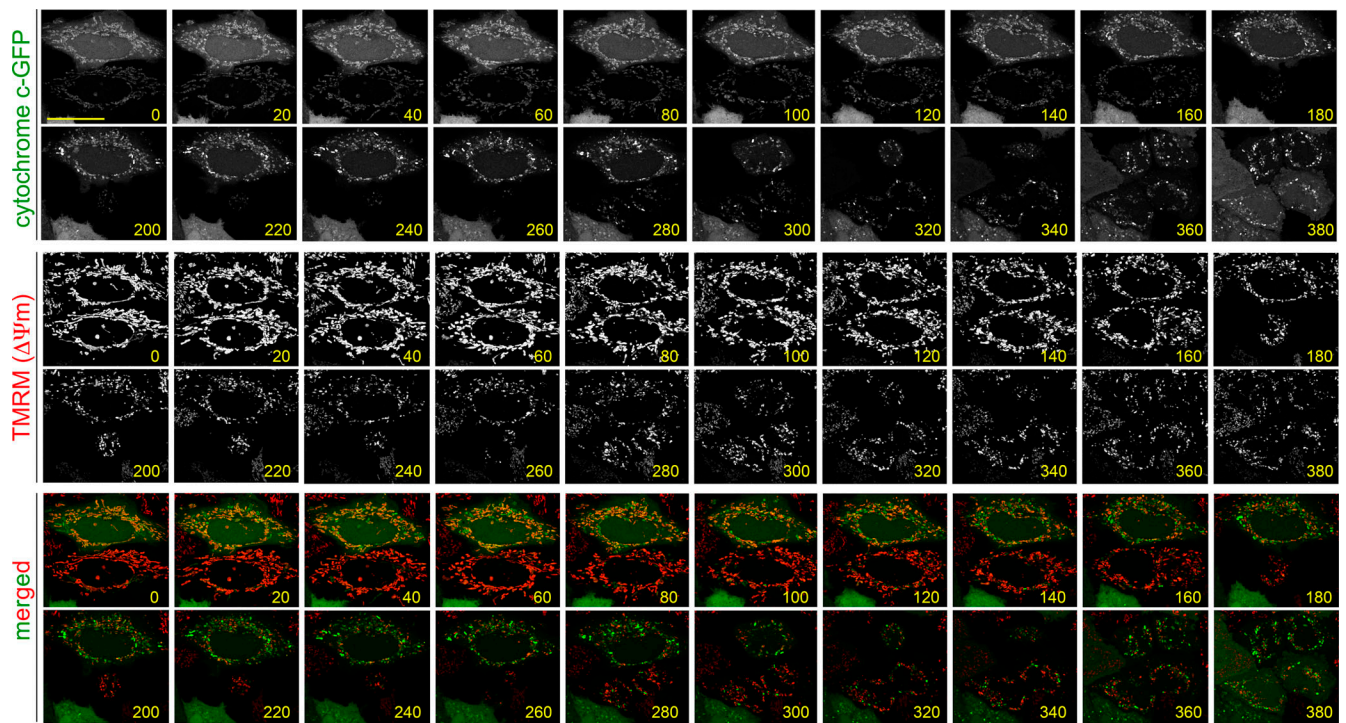


Figure S5. **Time-lapse imaging of mitochondrial membrane potential ($\Delta\Psi_m$) in Acn-treated HeLa cells.** WT HeLa cells transfected with cytochrome c-GFP (cyt. c-GFP) were loaded with TMRM, followed by Acn treatment. Images were acquired every 10 min (five z-sections with a 0.2- μm interval between sections) for up to 380 min. Scale bar represents 20 μm .

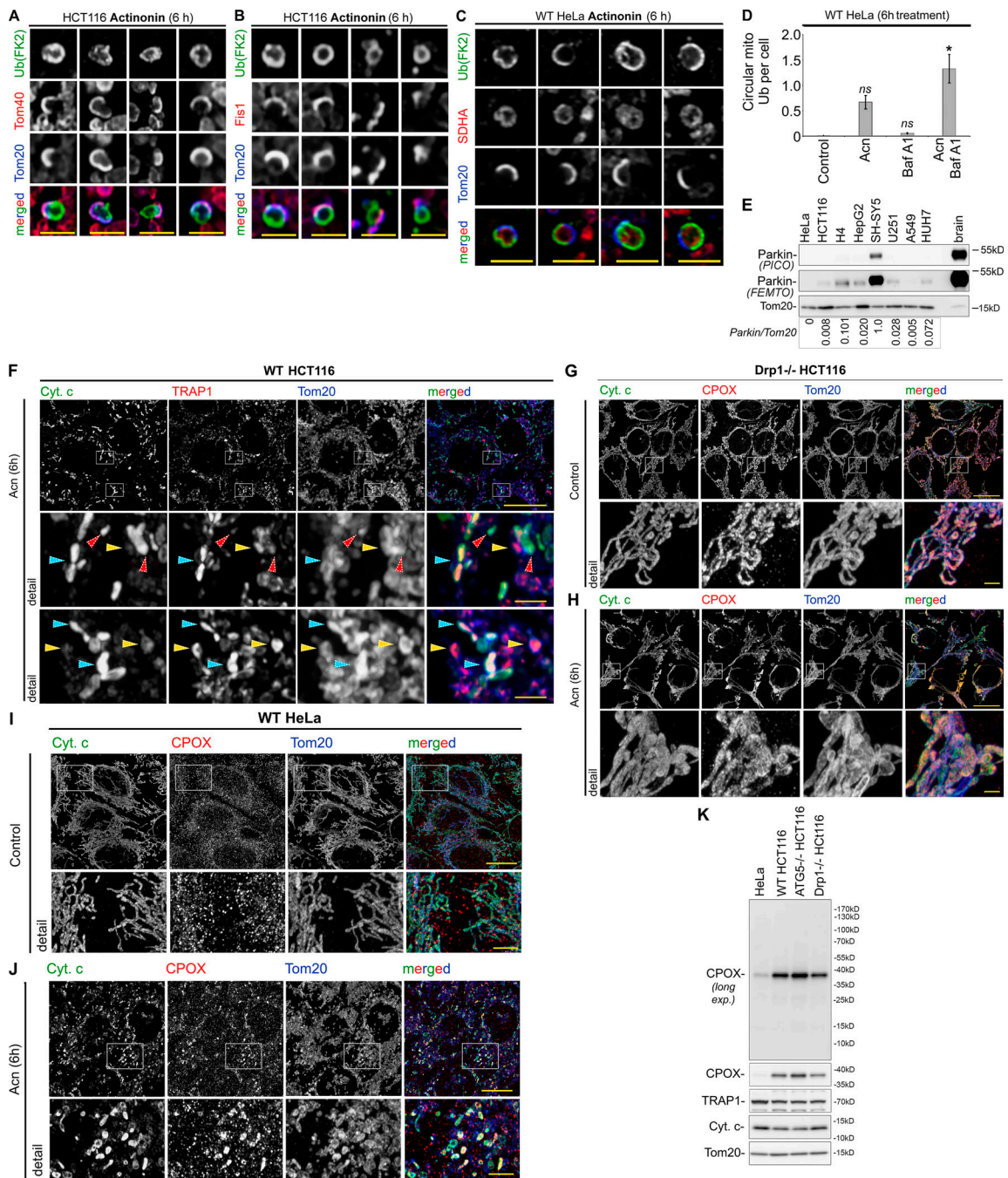


Figure S6. **OMM severing, IMM ubiquitination and distribution of TRAP1 and CPOX in Acn-treated HCT116 and HeLa cells. (A–C)** Examples of mitochondria with severed OMM from WT HCT116 (A and B) and WT HeLa (C) cells treated with Acn for 6 h and immunostained to detect conjugated Ub (FK2; green in A–C), Tom20 (blue in A–C), Tom40 (red in A), Fis1 (red in B), and SDHA (red in C). Scale bars represent 1 μ m. **(D)** Quantification of circular mitochondrial ubiquitination in WT HeLa cells treated as indicated in the figure. Data are represented by mean \pm SD; $n = 3$ ($n = 60$ cells per experiment). *, $P < 0.05$ versus control; ns indicates nonsignificant; Kruskal-Wallis with Dunn post-hoc analysis ($\alpha = 0.05$). **(E)** Total cell lysates obtained from HeLa (cervical adenocarcinoma), HCT116 (colorectal carcinoma), H4 (neuroglioma), HepG2 (hepatocellular carcinoma), SH-SY5Y (neuroblastoma), U251 (glioblastoma), A549 (lung epithelial carcinoma), and HU7 (hepatocellular carcinoma) were subjected to Western blot to detect Parkin. The upper “Parkin” panel show blots detected with a standard ECL detection reagent (Pico), and the Parkin panel second from the top was detected using a more sensitive ECL detection reagent (Femto). Rat brain lysate was included as a reference. Tom20 was used as loading control. Numbers in the bottom panel indicate expression of Parkin in all analyzed cells relative to SH-SY5Y neuroblastoma cells that showed the highest expression of this protein. The values were normalized to Tom20 levels. **(F–K)** Distribution and expression of TRAP1 and CPOX was analyzed in WT and Drp1^{-/-} HCT116 and WT HeLa cells. WT (F) and Drp1^{-/-} HCT116 (G and H) cells and WT HeLa cells (I and J) were treated with DMSO (G and I) or Acn (F, H, and J) for 6 h followed by immunostaining to detect cytochrome c (Cyt. c; green), Tom20 (blue), TRAP1 (red in F), and CPOX (red in G and H). Detail images are from areas marked with white rectangles. Scale bars represent 20 μ m in F–J; 2 μ m in detail images in F, G, and H; and 5 μ m in detail images in I and J. Arrowheads in F indicate mitochondria with high cytochrome c/low TRAP1 (red), high TRAP1/low cytochrome c (yellow), and high cytochrome c/high TRAP1 (blue). **(K)** Expression levels of CPOX, TRAP1, and cytochrome c in WT HeLa cells and WT, ATG5^{-/-}, and Drp1^{-/-} HCT116 cells was analyzed by Western blot. Tom20 was used as a loading control. Two exposures of CPOX blot are shown.

Video 1. **WT HeLa cells expressing mito-RED (red) and cyt. c-GFP (green) treated with Acn.**

Video 2. **Drp1^{-/-} HeLa cells expressing mito-RED (red) and cyt. c-GFP (green) treated with Acn.**

Video 3. **Mff^{-/-} HeLa expressing mito-RED (red) and cyt. c-GFP (green) treated with Acn.**

Video 4. **Drp1^{-/-} HeLa cells expressing Drp1-mCherry (red) and cyt. c-GFP (green) treated with Acn.**

Video 5. **WT HeLa cells expressing mito-RED (red) and cyt. c-GFP (green) treated with FCCP.**

Video 6. **TMRM-labeled WT HeLa cells expressing cyt. c-GFP (green) cotreated with Acn and CP.**

Video 7. **TMRM-labeled WT HeLa cells expressing cyt. c-GFP (green) treated with Acn.**

Video 8. **WT HeLa cells expressing Parkin-mCherry (red) and cyt. c-GFP (green) treated with Acn.**

A supplemental dataset, Data S1, showing original datasets from proteomic analyses of ubiquitinated proteins in membrane fractions from control or Acn-treated HCT116 cells, is available online.